Heat transfer in rapidly rotating convection with heterogeneous thermal boundary conditions

Jon E. Mound[1,†] and Christopher J. Davies[1,2]

[1]School of Earth and Environment, University of Leeds, Leeds LS2 9JT, UK

[2]Institute of Geophysics and Planetary Physics, Scripps Institution of Oceanography, University of California at San Diego, 9500 Gilman Drive, La Jolla, CA 92093-0225, USA

Convection in the metallic cores of terrestrial planets is likely to be subjected to lateral variations in heat flux through the outer boundary imposed by creeping flow in the overlying silicate mantles. Boundary anomalies can significantly influence global diagnostics of core convection when the Rayleigh number, Ra, is weakly supercritical; however, little is known about the strongly supercritical regime appropriate for planets. We perform numerical simulations of rapidly rotating convection in a spherical shell geometry and impose two patterns of boundary heat flow heterogeneity: a hemispherical Y_1^1 spherical harmonic pattern; and one derived from seismic tomography of the Earth's lower mantle. We consider Ekman numbers $10^{-4} \leqslant E \leqslant 10^{-6}$, flux-based Rayleigh numbers up to ~800 times critical, and a Prandtl number of unity. The amplitude of the lateral variation in heat flux is characterised by $q_L^* = 0$, 2.3, 5.0, the peak-to-peak amplitude of the outer boundary heat flux divided by its mean. We find that the Nusselt number, Nu, can be increased by up to ~25 % relative to the equivalent homogeneous case due to boundary-induced correlations between the radial velocity and temperature anomalies near the top of the shell. The Nu enhancement tends to become greater as the amplitude and length scale of the boundary heterogeneity are increased and as the system becomes more supercritical. This Ra dependence can steepen the $Nu \propto Ra^\gamma$ scaling in the rotationally dominated regime, with γ for our most extreme case approximately 20 % greater than the equivalent homogeneous scaling. Therefore, it may be important to consider boundary heterogeneity when extrapolating numerical results to planetary conditions.

Key words: Bénard convection, geophysical and geological flows, rotating flows

1. Introduction

Convection arises in many natural systems, from oceans and atmospheres to terrestrial mantles and liquid metal planetary cores. These systems often operate in dynamical regimes that cannot be attained in current laboratory experiments or numerical models. Significant effort has therefore focused on elucidating scaling relationships between the independent variables and diagnostics of the system

† Email address for correspondence: j.e.mound@leeds.ac.uk

behaviour. A particularly important diagnostic is the Nusselt number, *Nu*, a global measure of the efficiency of heat transport in the convecting system. This study is motivated by convection in low viscosity liquid metal planetary cores where rotation and the spherical geometry significantly affect the dynamics and convection in the overlying silicate mantles sets the thermal boundary conditions at the top of core. Lateral variations in the temperature field at the bottom of silicate mantles can be very large relative to those expected in the metallic cores, resulting in correspondingly large lateral variations in the thermal boundary conditions imposed on the underlying core. We focus here on the impact of such heterogeneous boundary conditions on the heat transfer behaviour of rapidly rotating convection in spherical geometry.

1.1. *Heat transport in convecting systems*

The canonical system used to understand convective heat transfer is a conducting fluid sandwiched between two parallel plates oriented normal to the gravity vector, with an imposed temperature difference ΔT across the layer. The system is characterised by the Rayleigh number, *Ra*, measuring the strength of the convective driving and the Prandtl number, $Pr = \nu/\kappa$, where ν is the kinematic viscosity and κ the thermal diffusivity. For a given value of *Pr*, as *Ra* is increased more heat is transported by advection and so $Nu = \epsilon Ra^{\gamma}$, with $\epsilon, \gamma > 0$. Malkus (1954) assumed that ΔT is accommodated predominantly by conduction in two identical thermal boundary layers at the top and bottom of the system; by further assuming that the local Rayleigh number of the boundary layer equals the critical value for stability he found that $Nu \propto Ra^{1/3}$. Numerical and physical experiments have produced a variety of scalings, which also depend on *Pr*. Grossmann & Lohse (2000) (see also Grossmann & Lohse 2001, 2002; Stevens *et al.* 2013) argued that these differences depend on whether the boundary layers or the bulk of the fluid dominate the kinematic and thermal dissipations, which divides *Ra–Pr* space into four regimes, each of which is divided into two subregimes based on the relative thickness of the thermal and kinetic boundary layers.

When the convecting system is rotating an additional non-dimensional parameter, the Ekman number, *E*, quantifies the relative strength of the viscous and Coriolis forces. The Coriolis force has a stabilising effect on the convection such that the critical Rayleigh number for the onset of convection, Ra_C, depends on *E*. When convection is geostrophic, that is the first-order force balance is between the Coriolis force and pressure gradients, a heat transport scaling of $Nu \propto Ra^3 E^4$ has been proposed (King, Stellmach & Aurnou 2012) following the same reasoning as Malkus (1954). However, in rapidly rotating systems a substantial interior temperature gradient can be maintained even to high *Ra* (Sprague *et al.* 2006; Julien *et al.* 2012*b*; King, Stellmach & Buffett 2013; Gastine, Wicht & Aubert 2016; Julien *et al.* 2016), which enhances diffusive heat transport and alters *Nu* relative to an equivalent non-rotating case. Experiments and numerical simulations in Cartesian geometry suggest that γ increases as *E* decreases into the rotationally dominated regime (Stellmach *et al.* 2014; Cheng *et al.* 2015). At $E = 10^{-7}$ a value of $\gamma = 3.6$ has been found, with no indication that the scaling had yet reached an asymptotic limit with reducing *E* (Cheng *et al.* 2015). Reduced equations valid in the asymptotic limit of small *E* (Sprague *et al.* 2006) also find $\gamma > 3$ at low *E* when the effect of Ekman pumping from no-slip boundary conditions is included (Stellmach *et al.* 2014; Aurnou *et al.* 2015; Julien *et al.* 2016; Plumley *et al.* 2016). Conversely, with free-slip boundary conditions the scaling at low-*E* appears to saturate with $\gamma = 3/2$, which is expected

for a turbulent quasi-geostrophic regime where the heat transport is independent of both the thermal and viscous diffusivities (Gillet & Jones 2006; Julien *et al.* 2012*a*; Stellmach *et al.* 2014).

In the spherical geometry considered in this paper, the boundary layer analysis is further complicated by asymmetric boundary layers, with the asymmetry in boundary layer thicknesses and temperature drops depending on both the radius ratio between the inner and outer boundaries and on the radial dependence of gravitational acceleration within the shell (Gastine, Wicht & Aurnou 2015). In the absence of rotation the *Nu–Ra* scaling in the shell is similar to that of the plane layer (Gastine *et al.* 2015). At sufficiently high *Ra* buoyancy forces will dominate Coriolis forces resulting in effectively non-rotating dynamics and *Nu–Ra* scaling. In the presence of rotation Gastine *et al.* (2016) obtained the diffusivity-free scaling $Nu \propto Ra^{3/2}E^2$ in a small region of parameter space with $E \lesssim 10^{-6}$ and $RaE^{4/3} \simeq 10$, conditions that placed the simulations in a dynamical regime that was both strongly nonlinear and dominated by rotation.

1.2. *Heterogeneous boundary conditions for the core*

Liquid metal planetary cores have higher thermal conductivity, and much lower viscosity, than their overlying solid silicate mantles. The resultant asymmetry in the thermal evolution of these systems implies that when considering thermal core–mantle interaction in simulations of core convection the use of fixed-flux boundary conditions would apply, whereas fixed-temperature boundary conditions would apply for the mantle (Olson 2003, 2016). Choosing fixed-temperature or fixed-flux boundary conditions results in different formulations of the Rayleigh and Nusselt numbers; these differences are outlined in § 2. However, after appropriate translation between the fixed-flux and fixed-temperature formulations the Nusselt–Rayleigh scaling is the same in both cases (Otero *et al.* 2002; Ahlers, Grossmann & Lohse 2009; Johnston & Doering 2009; Calkins *et al.* 2015; Goluskin 2015).

Mantle convection is much slower and supports much larger lateral variations in fluid properties (e.g. density, temperature, composition) than core convection (Olson 2003, 2016). It is therefore widely believed that convection in planetary cores must respond to a laterally varying pattern of heat flow imposed at the core–mantle boundary by mantle convection (Amit *et al.* 2015*a*). For the present-day Earth, a pattern of heat flux (figure 1*b*) is suggested by seismic tomography (e.g. Masters *et al.* 1996), which reveals two large low shear velocity provinces (LLSVPs) at the base of the mantle interpreted as hot, dense thermochemical piles in roughly antipodal locations beneath the Pacific Ocean and Africa (Garnero, McNamara & Shim 2016). Seismically fast material between these LLSVPs is interpreted as the cold remnant of subducted lithospheric slabs. The largest component of this tomographic pattern is spherical harmonic of degree and order two (Y_2^2), although other components also contribute. Inclusion of this pattern of heat flux in numerical models of the geodynamo can produce features in the spatial structure and temporal variation of the magnetic field similar to those observed for the Earth (Bloxham 2000; Olson & Christensen 2002; Gubbins, Willis & Sreenivasan 2007; Willis, Sreenivasan & Gubbins 2007; Davies *et al.* 2008; Amit, Aubert & Hulot 2010; Amit, Deschamps & Choblet 2015*b*; Olson 2016).

The present-day Earth is but one example of the pattern, and amplitude, of core–mantle boundary heat-flux heterogeneity that can arise in planetary mantle convection. During the assembly of super-continents, a primarily hemispheric (Y_1^1)
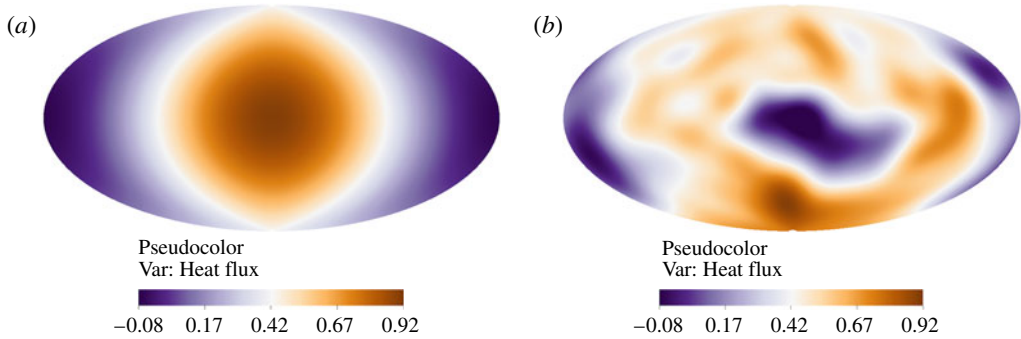
(*a*)   (*b*)

FIGURE 1. (Colour online) Patterns of core–mantle boundary heat flux with hemispheric (*a*) and tomographic (*b*) perturbations added to the mean. The projection is centred on the negative *x*-axis (the Pacific). In both cases $q_L^\star = 2.3$ and the choice of normalisation results in a mean heat flux of approximately 0.42; note that only the deepest purples are associated with a negative (i.e. radially inward) heat flux.

pattern of mantle convection and hence core–mantle boundary heat flux (figure 1*a*) may have existed (Zhong *et al.* 2007; Zhang & Zhong 2011; Olson *et al.* 2013; Olson 2016). A hemispheric heat-flux pattern has also been suggested for Mars to explain the Tharsis bulge (Zhong 2009; Šrámek & Zhong 2010), for the Moon to generate a non-axial magnetic field (Takahashi & Tsunakawa 2009; Oliveira & Wieczorek 2017), and for hot tidally locked terrestrial exoplanets (Gelman, Elkins-Tanton & Seager 2011).

The amplitude of the lateral variations in the heat flux conducted through the outer boundary can be expressed as

$$q_L^\star = \frac{q_{max} - q_{min}}{q_{ave} - q_{ad}}, \tag{1.1}$$

where q_{max}, q_{min} and q_{ave} are the maximum, minimum and horizontally averaged heat flux through the boundary, respectively, and q_{ad} is the heat flux conducted down the adiabatic gradient of the core at the boundary. $q_L^\star$ is challenging to precisely determine for Earth because it depends on the convective fluctuations as well as material properties of the mantle; it also will have varied through time. Estimates of the present-day total heat flow across the core–mantle boundary generally fall in the range $Q_{CMB} = 5$–20 TW (Lay, Hernlund & Buffett 2008; Nimmo 2015; Kavner & Rainey 2016). Mantle convection simulations predict $(q_{max} - q_{min})/q_{ave} = O(1)$ for Earth (Nakagawa & Tackley 2008; Olson *et al.* 2015). Recent upward revisions of the thermal conductivity of liquid iron mixtures increase q_{ad} so that it is comparable to estimates of q_{ave} (Lay *et al.* 2008; Davies 2015), in which case $q_L^\star \geqslant O(1)$. The lateral variations that we include in our model all have zero mean, therefore values of $q_L^\star > 2$ imply that for some portion of the outer boundary the heat flux is radially inward, although the integrated flux would remain outward. The average heat flux through the core–mantle boundary enters into the flux Rayleigh number for the core, for each flux Rayleigh number we will have a set of homogeneous and heterogeneous cases. Examples of the heat flux through the core–mantle boundary with $q_L^\star = 2.3$ are shown in figure 1 for both hemispheric and tomographic perturbations to the mean.

Numerical (Zhang & Gubbins 1993, 1996; Gibbons, Gubbins & Zhang 2007; Davies, Gubbins & Jimack 2009; Dietrich, Hori & Wicht 2016) and physical (Sumita & Olson 1999, 2002) experiments have investigated rotating convection with laterally

varying thermal boundary conditions for a variety of imposed patterns and $q_L^\star \ll 1$ up to $q_L^\star = O(1)$. The previous numerical work, conducted predominantly at Ra a few times critical, has shown that imposed boundary heterogeneity can have a substantial influence on the spatial patterns and time dependence of convection in the fluid shell, particularly when the wavelength of the imposed pattern is large. However, to our knowledge, the only previous study that compared heat transfer behaviour in rotating spherical shells with and without heterogeneous outer boundary forcing was that of Dietrich *et al.* (2016) who carried out simulations of internally heated rotating spherical shell convection with a Y_1^1 outer boundary heat-flux pattern at $Pr = 1$ and $E = 2.5, 5 \times 10^{-5}$ (using the definition of E in § 2.1) and flux-based Rayleigh numbers up to 400 times critical for $E = 5 \times 10^{-5}$. Estimating ΔT based on the maximum and minimum values of T in the domain Dietrich *et al.* (2016) found that Nu is reduced by up to 50 % from the homogeneous case as the amplitude of heterogeneity is increased up to $q_L^\star = 2$ (using our definition (1.1)).

Here we present results from 106 numerical simulations of bottom-heated rotating convection in a spherical shell with values of E as low as 10^{-6}. We include two patterns of boundary heterogeneity and extend to flux-based Rayleigh numbers several hundred times critical. We focus in particular on heat transport within these models and the impact of the boundary heterogeneity on Nu as a measure of convective efficiency. In § 2 we outline our theoretical basis for exploring heat transport in rotating convection; in § 3 we present summary results of all of our numerical simulations and more extended discussion of certain illustrative cases.

2. Theory

2.1. *Governing equations and non-dimensionalisation*

We employ a numerical model of convection of a homogeneous Boussinesq fluid confined within a rotating spherical shell (Willis *et al.* 2007). The fluid is characterised by its constant thermal diffusivity, κ, kinematic viscosity, ν, coefficient of thermal expansion, α, and reference density, ρ_0. The thermal diffusivity can be expressed as $\kappa = k/\rho_0 C_P$, where k is the thermal conductivity and C_P the heat capacity of the fluid. The shell is defined in spherical coordinates, (r, θ, ϕ), by the inner and outer boundaries, r_i and r_o, respectively, and rotates with a constant angular velocity $\boldsymbol{\Omega} = \Omega \hat{\boldsymbol{z}}$. The governing equations for conservation of momentum, energy and mass can be written

$$\left(\frac{\partial \boldsymbol{u}}{\partial t} + (\boldsymbol{u} \cdot \nabla)\boldsymbol{u} \right) + 2\boldsymbol{\Omega} \times \boldsymbol{u} = -\frac{1}{\rho_0}\nabla \widetilde{P} + \frac{\rho}{\rho_0}\boldsymbol{g} + \nu \nabla^2 \boldsymbol{u}, \quad (2.1)$$

$$\frac{\partial T}{\partial t} + (\boldsymbol{u} \cdot \nabla)T = \kappa \nabla^2 T, \quad (2.2)$$

$$\nabla \cdot \boldsymbol{u} = 0. \quad (2.3)$$

The modified pressure, $\widetilde{P}$, includes the centrifugal potential. Gravity varies linearly with radius such that $\boldsymbol{g} = -(g_o/r_o)\boldsymbol{r}$, where g_o is the gravitational acceleration at $r = r_o$.

The fluid is incompressible (2.3) and so the velocity, $\boldsymbol{u}$, can be decomposed into toroidal, $\mathcal{T}$, and poloidal, $\mathcal{P}$, components such that

$$\boldsymbol{u} = \nabla \times (\mathcal{T}\hat{\boldsymbol{r}}) + \nabla \times \nabla \times (\mathcal{P}\hat{\boldsymbol{r}}). \quad (2.4)$$

The toroidal and poloidal scalar fields can then be expressed in terms of spherical harmonics, Y_ℓ^m, with radially varying harmonic coefficients $\tau_\ell^m(r)$ and $p_\ell^m(r)$ respectively.

In this work we make use of the Schmidt semi-normalised spherical harmonics common in geomagnetic studies (e.g. Kono 2015). The boundary conditions on the velocity are non-penetrative and no slip such that $\boldsymbol{u} = 0$ on $r = r_i, r_o$.

The temperature field, T, can be written as

$$T = T_C + T', \tag{2.5}$$

where T_C is the steady-state temperature in the absence of flow and T' is the fluctuation about this state. We denote the coefficients of the spherical harmonic expansion of T by $\vartheta_\ell^m(r)$. Fixed-flux thermal boundary conditions are imposed such that $\nabla T_C = -(\beta/r^2)\hat{\boldsymbol{r}}$ at the inner and outer boundaries. Thus the total heat flow, Q, is equal through the inner and outer surfaces and, for example, on the outer boundary

$$Q = 4\pi r_o^2 q_{ave} = 4\pi r_o^2(-k\nabla T_C) = 4\pi k\beta. \tag{2.6}$$

We introduce the following notation for radial, spherical surface and time averages, respectively

$$\{f(r)\} = \frac{1}{h} \int_{r_i}^{r_o} f(r) \, \mathrm{d}r, \tag{2.7}$$

$$\langle f(r, \theta, \phi) \rangle = \frac{1}{4\pi r^2} \int_0^\pi \int_0^{2\pi} f(r, \theta, \phi) r^2 \sin\theta \, \mathrm{d}\phi \, \mathrm{d}\theta, \tag{2.8}$$

$$\overline{f(t)} = \frac{1}{\tau} \int_{t_0}^{t_0+\tau} f(t) \, \mathrm{d}t, \tag{2.9}$$

where $h = r_o - r_i$ is the shell thickness and τ is the duration of the time averaging.

The control parameters that characterise the convecting system are derived from non-dimensionalisation of the governing equations (2.1)–(2.3). We scale length by the shell thickness, h, time by the thermal diffusion time, $\tau_d = h^2/\kappa$, and temperature by β/h. With this choice of scaling the Ekman number, Prandtl number and modified Rayleigh number can be defined as

$$E = \frac{\nu}{2\Omega h^2}, \quad Pr = \frac{\nu}{\kappa}, \quad \widetilde{Ra} = \frac{\alpha g_o \beta}{2\Omega\kappa}, \tag{2.10a–c}$$

and the resultant non-dimensional governing equations are

$$\frac{E}{Pr}\left(\frac{\partial \boldsymbol{u}^\star}{\partial t^\star} + (\boldsymbol{u}^\star \cdot \nabla^\star)\boldsymbol{u}^\star\right) + \hat{\boldsymbol{z}} \times \boldsymbol{u}^\star = -\nabla^\star \widetilde{P^\star} + \widetilde{Ra} T'^\star \boldsymbol{r}^\star + E\nabla^{\star 2}\boldsymbol{u}^\star, \tag{2.11}$$

$$\frac{\partial T^\star}{\partial t^\star} + (\boldsymbol{u}^\star \cdot \nabla^\star)T^\star = \nabla^{\star 2}T^\star, \tag{2.12}$$

$$\nabla^\star \cdot \boldsymbol{u}^\star = 0. \tag{2.13}$$

In all of our models $Pr = 1$ and the radius ratio of the shell is set to $r_i/r_o = 0.35$, the value for Earth's core. The modified Rayleigh number is related to a flux Rayleigh number by

$$Ra_F = \frac{\alpha g_o \beta h^2}{\nu\kappa} = \frac{\widetilde{Ra}}{E}. \tag{2.14}$$

To convert from flux-based to temperature-based Rayleigh number we need to relate β to the temperature drop across the convecting system, ΔT. The solution to the

spherical shell conduction problem (see (2.22)–(2.25) below) gives $\beta = \Delta T_C r_i r_o / h$, which in combination with our expression for the Nusselt number ((2.30) below) leads to

$$Ra_T = \frac{\alpha g_o \Delta T h^3}{\nu \kappa} = \frac{Ra_F}{Nu} \frac{h^2}{r_i r_o}, \tag{2.15}$$

where ΔT is taken to be $\overline{\Delta \langle T \rangle}$, the measured time-averaged temperature drop across the convecting system.

Below we will generally present results relative to the advection time scale, $\tau_a = h/U$, where U is a characteristic velocity for the flow. The ratio between thermal diffusion and advection time scales is the thermal Péclet number, $Pe = \tau_d / \tau_a = Uh/\kappa$. The thermal Péclet number is the product of the Prandtl and Reynolds numbers; since we set $Pr = 1$ in all of our models we have $Pe = Re = Uh/\nu$. The characteristic velocity is derived from the kinetic energy and after non-dimensionalisation we have

$$Pe = Re = U^\star = \sqrt{\frac{2KE^\star}{Vs^\star}}, \tag{2.16}$$

where $Vs^\star$ is the non-dimensional volume of the domain and $KE^\star$ is the non-dimensional kinetic energy of the system defined by

$$KE^\star = \tfrac{1}{2} \iiint_{Vs^\star} \overline{\boldsymbol{u}^{\star 2}} \, \mathrm{d}V^\star. \tag{2.17}$$

2.2. *Heat transport*

The Nusselt number provides a global measure of the efficiency of heat transport in a convecting system by comparing the total heat flux through the system to that which could be transferred by conduction alone. Equation (2.2) can be written as

$$\rho_0 C_P \frac{\partial T}{\partial t} + \boldsymbol{\nabla} \cdot \boldsymbol{q} = 0, \tag{2.18}$$

where the total heat flux

$$\boldsymbol{q} = \rho_0 C_P \boldsymbol{u} T - k \boldsymbol{\nabla} T \tag{2.19}$$

is the sum of the advective and diffusive contributions.

We first revisit the canonical example of a plane layer of thickness of d and fixed temperature difference across the layer of ΔT. In this case the Nusselt number is

$$Nu = \frac{\langle \overline{\boldsymbol{q}} \cdot \hat{\boldsymbol{z}} \rangle}{k \Delta T / d}, \tag{2.20}$$

where the total vertical heat flux, $\boldsymbol{q} \cdot \hat{\boldsymbol{z}}$, can be averaged over any horizontal surface and the conduction solution gives $(\boldsymbol{\nabla} T_C) \cdot \hat{\boldsymbol{z}} = -\Delta T / d$. It can be particularly useful to consider the top or bottom surface, where $\boldsymbol{q} \cdot \hat{\boldsymbol{z}}$ is purely conductive, such that the Nusselt number can be written

$$Nu = \frac{-\langle (\boldsymbol{\nabla} \overline{T}) \cdot \hat{\boldsymbol{n}} \rangle |_{top}}{-(\boldsymbol{\nabla} T_C) \cdot \hat{\boldsymbol{n}} |_{top}} = \frac{\langle (\boldsymbol{\nabla} \overline{T}) \cdot \hat{\boldsymbol{n}} \rangle |_{bottom}}{(\boldsymbol{\nabla} T_C) \cdot \hat{\boldsymbol{n}} |_{bottom}}, \tag{2.21}$$

where $\hat{\boldsymbol{n}}$ is the outward normal with respect to the domain.

In numerical or physical experiments with fixed-temperature boundary conditions the Nusselt number can thus be evaluated by determining $\langle \overline{\boldsymbol{q}} \cdot \hat{\boldsymbol{n}} \rangle$ for a sufficiently large averaging time. Fixed-flux boundary conditions set $\nabla T = \nabla T_C$ on both boundaries at every instant in time, in which case (2.21) suggests $Nu = 1$ regardless of convective vigour. Although the non-penetration condition requires that all heat is transferred by conduction across the boundaries, within the fluid interior the advective heat transport will reduce the temperature gradient. In experiments where $\langle \overline{\boldsymbol{q}} \cdot \hat{\boldsymbol{n}} \rangle$ is fixed, the temperature drop across the system is the quantity to be determined in (2.20).

In our model, with fixed-flux boundaries and spherical shell geometry, the conduction problem is

$$\frac{\kappa}{r^2} \frac{\mathrm{d}}{\mathrm{d}r} \left(r^2 \frac{\mathrm{d}T_C}{\mathrm{d}r} \right) = 0, \tag{2.22}$$

subject to boundary conditions

$$\left. \frac{\mathrm{d}T_C}{\mathrm{d}r} \right|_{r=r_o} = -\frac{\beta}{r_o^2}, \quad \left. \frac{\mathrm{d}T_C}{\mathrm{d}r} \right|_{r=r_i} = -\frac{\beta}{r_i^2}. \tag{2.23a,b}$$

The solution is

$$\frac{\mathrm{d}T_C}{\mathrm{d}r} = -\frac{\beta}{r^2}, \quad T_C = \frac{\beta}{r} + B, \tag{2.24a,b}$$

where B is a constant of integration that is not constrained by the flux boundary conditions. Therefore, the temperature drop across the shell in the conduction only case is

$$\Delta T_C = \beta \left(\frac{1}{r_i} - \frac{1}{r_o} \right) = \frac{\beta h}{r_i r_o}. \tag{2.25}$$

The total heat flux of the convecting system is found by time averaging equation (2.18) for a duration that is sufficiently long to reach a statistical steady state, in which case $\nabla \cdot \overline{\boldsymbol{q}} = 0$ within the domain, a consequence of the absence of internal heat sources. It follows that

$$\iiint_{V_s} \nabla \cdot \overline{\boldsymbol{q}} \, \mathrm{d}V = 0 = \oint \overline{\boldsymbol{q}} \cdot \hat{\boldsymbol{n}} \, \mathrm{d}S = 4\pi r_o^2 \langle \overline{\boldsymbol{q}} \cdot \hat{\boldsymbol{r}} \rangle|_{r=r_o} - 4\pi r_i^2 \langle \overline{\boldsymbol{q}} \cdot \hat{\boldsymbol{r}} \rangle|_{r=r_i} \tag{2.26}$$

and, since the volume of integration is arbitrary, $4\pi r^2 \langle \overline{\boldsymbol{q}} \cdot \hat{\boldsymbol{r}} \rangle$ is independent of r. The imposed boundary conditions require $u_r|_{r=r_i} = u_r|_{r=r_o} = 0$, $\partial \overline{T}/\partial r|_{r=r_o} = -\beta/r_o^2$, and $\partial \overline{T}/\partial r|_{r=r_i} = -\beta/r_i^2$, therefore

$$4\pi r^2 \langle \overline{\boldsymbol{q}} \cdot \hat{\boldsymbol{r}} \rangle = 4\pi r_o^2 \langle -k\partial \overline{T}/\partial r \rangle|_{r=r_o} = 4\pi r_i^2 \langle -k\partial \overline{T}/\partial r \rangle|_{r=r_i} = 4\pi k\beta \tag{2.27}$$

and

$$\langle \overline{\boldsymbol{q}} \cdot \hat{\boldsymbol{r}} \rangle = k\beta/r^2 = -k(\mathrm{d}T_C/\mathrm{d}r). \tag{2.28}$$

Although $4\pi r^2 \langle \overline{\boldsymbol{q}} \cdot \hat{\boldsymbol{r}} \rangle$ is independent of r, the advective and diffusive contributions to the total radial heat flux will vary. The global balance between the advective and diffusive contributions requires integration with respect to r, leading to the following expression for the Nusselt number based on fluxes

$$Nu_F = \frac{\{\langle \overline{\boldsymbol{q}} \cdot \hat{\boldsymbol{r}} \rangle\}}{\{\langle -k\partial \overline{T}/\partial r \rangle\}}. \tag{2.29}$$

Using (2.28) allows us to recast Nu_F as

$$\frac{-\dfrac{k}{h}\displaystyle\int (dT_C/dr)\,dr}{-\dfrac{k}{h}\displaystyle\int (d\langle\overline{T}\rangle/dr)\,dr} = \frac{\Delta T_C}{\Delta\langle\overline{T}\rangle} = Nu_T. \tag{2.30}$$

The order of the horizontal and temporal averaging in $\Delta\langle\overline{T}\rangle$ is interchangeable and in practice we determine $\overline{\Delta\langle T\rangle}$. Note that when considering the non-dimensional form of (2.30) our geometry and choice of temperature scaling results in $\Delta T_C^\star \approx 1.2$ rather than unity, as would be typical for Cartesian geometry (e.g. Otero *et al.* 2002; Goluskin 2015) (see also appendix A).

Let us consider the implications of a change in Nusselt number between two models with the same value of Ra_F but different patterns or amplitudes of boundary heat-flux variation. Equation (2.30) shows that a change in Nu corresponds to a change in the temperature drop across the system since ΔT_C is set by β (recall (2.25)), and hence by Ra_F. Furthermore, equations (2.19) and (2.28) imply that any change in $\langle\partial\overline{T}/\partial r\rangle$ must be compensated by a complementary change in $\langle\overline{u_r T}\rangle$. Changing the efficiency of heat transport requires alteration of both the temperature and velocity fields.

The time-averaged temperature drop across the system can be expressed using the spherical harmonic expansion of the temperature field as

$$\Delta\langle\overline{T}\rangle = \overline{\vartheta_0^0(r_i)} - \overline{\vartheta_0^0(r_o)}; \tag{2.31}$$

any change in Nu_T induced by the heterogeneous boundary condition must influence the Y_0^0 spherical harmonic component of the temperature field. The imposed patterns of boundary heterogeneity have zero mean and hence the homogeneous and heterogeneous thermal boundary conditions have identical Y_0^0 components for a given Ra_F. Since there is no interaction between harmonics in the diffusive part of the energy equation (2.2), any change in $\overline{\Delta T}$, and hence $\vartheta_0^0(r)$, must arise from nonlinear interaction between the flow and temperature fields. This can be seen by writing equation (2.28) as

$$\overline{\langle u_r T\rangle} = \kappa\frac{d}{dr}\left(\overline{\vartheta_0^0} - T_C\right). \tag{2.32}$$

The radial component of velocity depends only on the poloidal component of the velocity field, thus spherical harmonic expansion of the variables on the left-hand side of (2.32) leads to

$$\frac{1}{r}\sum_{\ell,m}\left(\frac{\ell(\ell+1)}{2\ell+1}\right)\overline{p_\ell^m\vartheta_\ell^m} = \kappa\frac{d}{dr}\left(\overline{\vartheta_0^0} - T_C\right), \tag{2.33}$$

where we have made use of the orthogonality of the (Schmidt-normalised) spherical harmonics. Equation (2.3) implies that $p_0^0 = 0$ and thus we see that ϑ_0^0 must be modified by interactions between flow and temperature at other harmonics.

Consider, for example, a homogeneous model to which is added a Y_1^1 heat-flux heterogeneity at the outer boundary. In this case we anticipate that the heat-flux heterogeneity will increase $\overline{\vartheta_1^1}$ near the top of the fluid core, relative to the homogeneous boundary case. This temperature perturbation in the core then generates,

on average, some amount of p_1^1 flow by promoting (inhibiting) downwelling in regions of enhanced (reduced) outward heat flux across the boundary. Any resultant increased correlation between the hemispheric patterns in radial flow and temperature (i.e. an increase in $\overline{p_1^1 \vartheta_1^1}$ for radii near r_o) implies an altered $\mathrm{d}\overline{\vartheta_0^0}/\mathrm{d}r$ and hence Nu_T. Correlations at harmonics other than those of the imposed heterogeneity could also be promoted by the boundary heterogeneity through some more complex set of dynamics. Regardless, for fixed Ra_F the total heat transport through the system remains unchanged and an increase in Nu with heterogeneous boundary conditions, which reflects a repartitioning of heat transport from conduction to advection, requires an increased correlation between u_r and T and a smaller average radial temperature gradient. This reorganisation of flow and temperature fields could occur throughout the domain or be limited to a relatively restricted region, for example near the outer boundary. In the following section we present the heat transport results for our suite of models. We will not present a detailed analysis of the association between flow and Nu for all simulations, but any case for which the heterogeneous boundary conditions have altered Nu relative to the equivalent homogeneous case must have some reorganisation of the time-averaged flow in accordance with the principles outlined here.

3. Results and discussion

3.1. *Numerical model, parameters and convergence tests*

The pseudo-spectral method used in this work is described in Willis *et al.* (2007); it passes the dynamo benchmark and performs comparably to other pseudo-spectral methods (Matsui *et al.* 2016). The velocity field is decomposed into toroidal and poloidal scalars, which ensures that the divergence-free condition is satisfied exactly. All scalars are then expanded in Schmidt-normalised spherical harmonics on each spherical surface and represented in radius by second-order finite differences. The finite difference points are located at the zeros of the Chebyshev polynomials, providing finer spacing near the upper and lower boundaries. Time stepping is accomplished in spectral space using a predictor–corrector scheme that treats diffusion terms implicitly, while the Coriolis, buoyancy and nonlinear terms are treated explicitly. Nonlinear terms are transformed into real space at each time step using the spherical transform method (Orszag 1971). At each radius multiplications are performed on a Gauss–Legendre grid with $(3/2)\ell_{max}$ colatitude points and $3\ell_{max}$ longitude points. The number of radial grid points, N_r, and the maximum spherical harmonic degree and order, $\ell_{max} = m_{max}$, for all runs are given in appendix B. Our choices of ℓ_{max} are similar to those used by Gastine *et al.* (2016) for comparable control parameters.

In this work we focus on the global heat transport of rotating convection in a spherical shell with variable heat-flux boundary conditions. To do so we have run a suite of 106 numerical simulations with: Ekman number, $E = 10^{-4}$, 10^{-5}, 10^{-6}; flux Rayleigh number, $3 \times 10^5 \leqslant Ra_F \leqslant 1.8 \times 10^{10}$; Prandtl number, $Pr = 1$. Strong rotation inhibits the onset of convection; for our thermal and mechanical boundary conditions, and choices of Ekman and Prandtl numbers, linear stability analysis of the homogeneous cases (for details see Gibbons *et al.* 2007; Davies *et al.* 2009) indicates that our simulations fall in the range $1.2Ra_C \lesssim Ra_F \lesssim 800Ra_C$ (the critical Rayleigh number, $\widetilde{Ra}_C$, and most unstable mode at onset, m_C, for our cases are given in table 1). The control and output parameters for all runs are detailed in appendix B.

E	$\widetilde{Ra}_C$	m_C
10^{-4}	16.4	5
10^{-5}	24.7	12
10^{-6}	41.0	25

TABLE 1. Critical Rayleigh number and critical azimuthal wavenumber for our simulations.
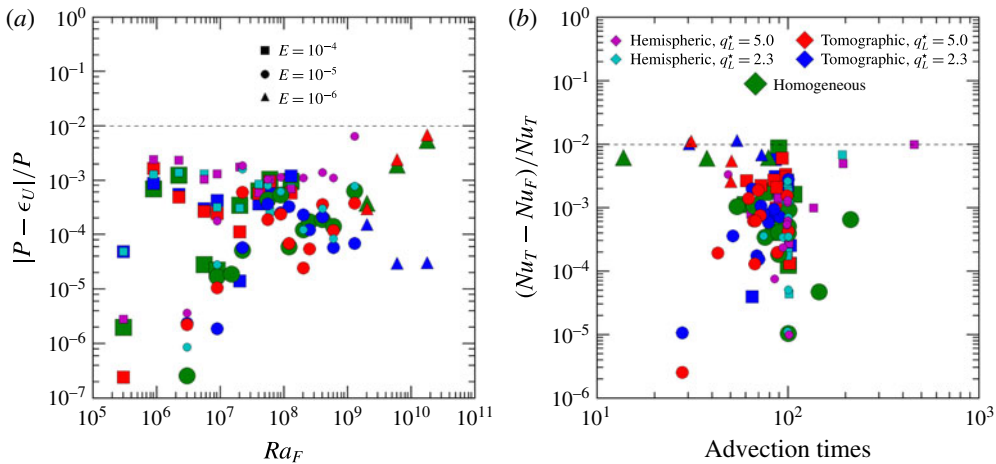

FIGURE 2. (Colour online) (*a*) Convergence of all models as measured by the difference between the time average of the buoyancy production, P, and viscous dissiaption, ϵ_U, both integrated over the volume of the shell. (*b*) Convergence of the time-averaged Nusselt number for all models as measured by the difference between $\overline{Nu_F}$ and $\overline{Nu_T}$. Symbol shapes indicate the value of E, symbol size and colour indicate the nature of the boundary conditions.

We consider three different patterns of heat flux imposed at the outer boundary. Simulations with a homogeneous outer boundary have $q_L^\star = 0$. Cases with the hemispheric pattern described by the Y_1^1 spherical harmonic (figure 1*a*) are referred to using $Hq_L^\star$, in these simulations q_{max} (q_{min}) is aligned with the negative (positive) x axis. Cases with boundary heterogeneity derived from the observed pattern of seismic velocity variations in the lowermost mantle (Masters *et al.* 1996) (figure 1*b*) are referred to using $Tq_L^\star$. The amplitude of the heat-flux heterogeneity is set to $Hq_L^\star$, $Tq_L^\star = 2.3$ or 5.0; values based on a proposed scaling from seismic velocity to temperature following the work of Nakagawa & Tackley (2008).

The spatial convergence of each simulation is evaluated by checking that the buoyancy production throughout the volume, P, is matched by the viscous dissipation, ϵ_U, in the time average (see e.g. Gastine *et al.* 2015). Figure 2(*a*) shows $|P - \epsilon_U|/P$ for all cases, this residual is always less than 10^{-2}. We compute the thickness of the viscous boundary layers at $r = r_i, r_o$ based on the location of the local maxima in the radial profile of horizontal velocity variations following the method described in King *et al.* (2013) and report the number of grid points within the boundary layers for each simulation in appendix B. With one exception, there are at least 7 points in both boundary layers and the majority of simulations have many more points than this (the lowest Rayleigh homogeneous model at $E = 10^{-5}$ has 28 radial grid points
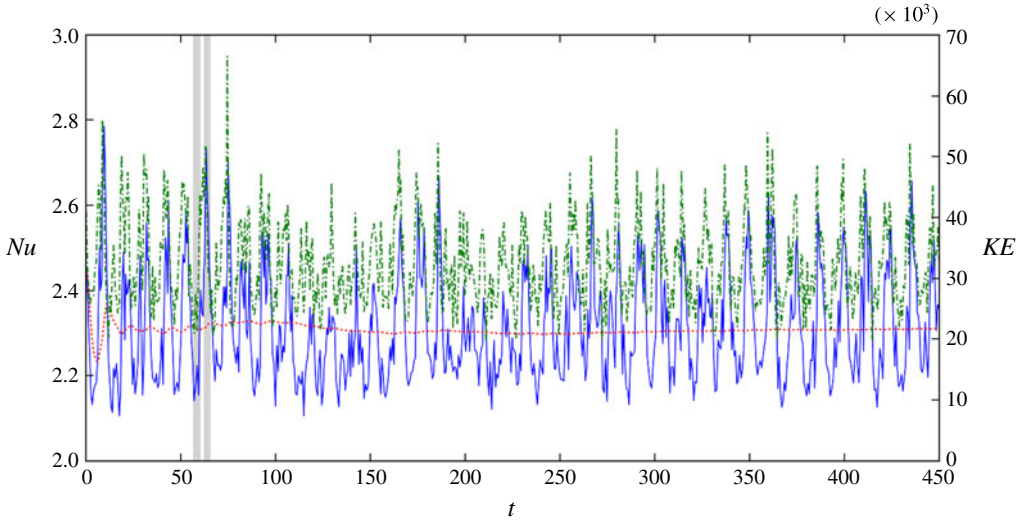
FIGURE 3. (Colour online) $KE^{\star}$ (dash-dot green line, right-hand axis), Nu_T (blue solid line, left-hand axis), and the running average of Nu_T (dotted red line, left-hand axis) for the run with $E = 10^{-4}$, $Ra_F = 2.25 \times 10^6$ and $Hq_L^{\star} = 5.0$. The representative flow patterns for the low- and high-Nu states shown in figure 4 were found by averaging over the time periods indicated by the grey shading. Time is measured by the advection time scale.

within the boundary layer near r_i, but only 5 within the boundary layer near r_o). These boundary layer resolutions are comparable to those used by Stevens, Verzicco & Lohse (2010) for resolving the radial structure of thermal boundary layers in Rayleigh–Bénard convection.

After removal of the initial transient, time averages are constructed over a span of at least 10 advection times and in general of around 100 advection times. The Reynolds number allows conversion from advection to diffusion times; the durations of the runs mostly lie between 0.01 and 10 diffusion times. Convergence of the Nusselt number is tested by considering the difference between $\overline{Nu_F}$ and $\overline{Nu_T}$ as determined by time averaging over the run. As shown in figure 2(b) the difference between these two methods of calculating the Nusselt number is of the order of 1 % or less.

The case with $E = 10^{-4}$, $Ra_F = 2.25 \times 10^6$ and $Hq_L^{\star} = 5.0$ (the rightmost point in figure 2b) required over 450 advection times to reach our 1 % convergence target, significantly longer than the other runs. The kinetic energy and instantaneous Nu time series for this case display large amplitude fluctuations (figure 3). The system switches between two states each of which persists for several advection times, with times of higher (lower) $KE^{\star}$ correlated with periods of higher (lower) Nu; $Re = 67.3$ for this run, so the period of the oscillations is approximately 0.1 diffusion times. There is a time lag between the total and zonal kinetic energies of the system suggesting that the convection generates progressively stronger zonal flow until the resultant shear disrupts the convective rolls. Similar relaxation oscillations have been seen in homogeneous rotating spheres (see e.g. Busse 2002, for a review), here the boundary heterogeneity modulates convection activity such that localised convection is concentrated in the hemisphere that is most strongly cooled by the overlying mantle.

Representative flow patterns for the low- and high-Nu states were found by averaging over the time periods indicated by the grey shading in figure 3, each
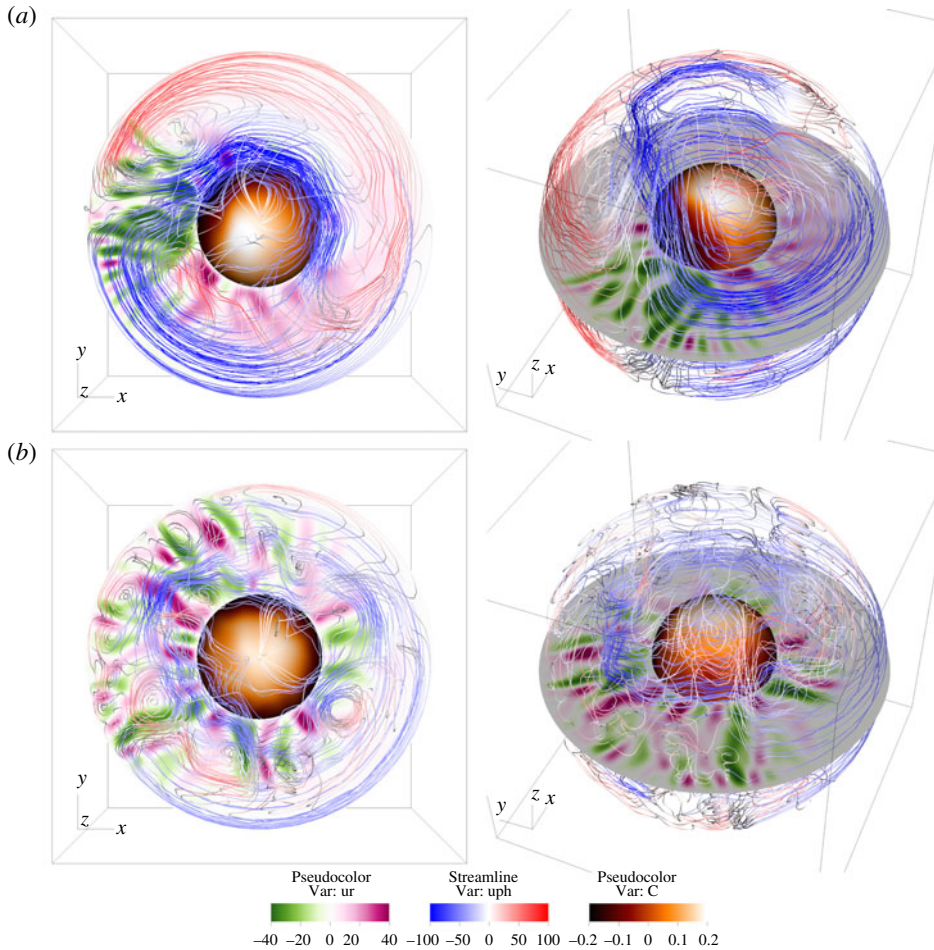
FIGURE 4. (Colour online) Time-averaged flows for the run with $E = 10^{-4}$, $Ra_F = 2.25 \times 10^6$, and $Hq_L^\star = 5.0$ averaged over a period of high Nu (a) and a period of low Nu (b), the averaging periods are indicated by the grey bands in figure 3. The equatorial plane is coloured by $u_r^\star$ in the plane (green–magenta), streamlines of the time-averaged velocity field are coloured by $u_\phi^\star$ (blue–red), and the inner boundary is coloured by temperature anomaly relative to the horizontal average (brown–orange–white). On the outer boundary q_{min} is aligned with the positive x-axis and q_{max} is aligned with the negative x-axis. The rotation vector points in the positive z direction.

of which corresponds to approximately three advection times. The flow pattern in the low-Nu state (figure 4b) consists of a well-developed zonal flow in the shell interior interacting with convective rolls aligned with the rotation axis. Relatively hot fluid accumulates near the outer boundary in the positive x hemisphere below q_{min}, which tends to suppress the formation of convective rolls, and hence radial flow, above mid-depth in that hemisphere. Conversely, q_{max} in the negative x hemisphere tends to enhance radial flow. The high-Nu state (figure 4a) is characterised by two large-scale circulations anchored by a large downwelling beneath q_{max}. Peak upwelling velocities in the high-Nu state are similar to those of the low-Nu state; however, peak downwelling velocities have approximately 50 % greater amplitude. The strong

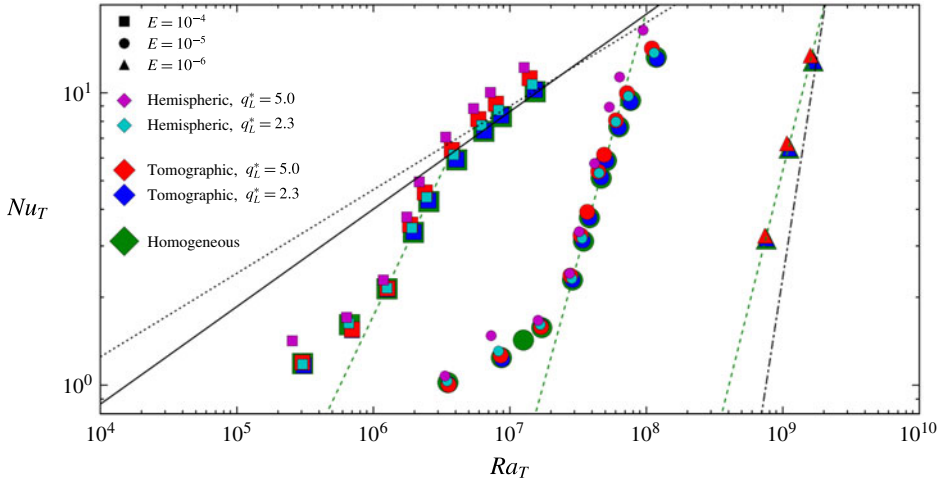FIGURE 5. (Colour online) Scaling of Nu_T against Ra_T. Dashed green lines are fits to the Ra homogeneous cases, giving $Nu \propto Ra_T^{0.98}$, $Nu \propto Ra_T^{1.69}$ and $Nu \propto Ra_T^{1.86}$ for $E = 10^{-4}$, $E = 10^{-5}$ and $E = 10^{-6}$, respectively. For comparison, black lines are scalings of $Nu \propto Ra_T^{1/3}$ (solid) and $Nu \propto Ra_T^{2/7}$ (dotted) for non-rotating convection and $Nu \propto Ra_T^3 E^4$ for rotationally constrained convection (dash-dot, for $E = 10^{-6}$). Symbol shapes indicate the value of E, symbol size and colour indicate the nature of the boundary conditions.

downwelling is relatively effective at transporting cold material deep within the shell such that the high-Nu state has a long-wavelength azimuthal temperature anomaly at the equator of the inner boundary, in addition to the general pattern of positive (negative) temperature anomalies at high (low) latitudes seen at all times in this model. The higher average velocities and changed pattern of convection increase the global correlation between radial velocity and temperature and correspondingly reduce the average temperature drop across the shell during the high-$KE^\star$–high-Nu state.

3.2. *Nusselt–Rayleigh scaling*

Figure 5 plots Nu_T against Ra_T for all of our simulations. For a given value of E the slope of the Nu–Ra_T scaling is shallow at relatively low Ra in the weakly nonlinear regime, steepens as the Rayleigh number increases, and shallows again at the highest values of Ra_T, particularly for the runs with $E = 10^{-4}$ (see also figures 6 and 7 for plots of several compensated Nu scalings). Due to the computational expense we have performed a limited number of runs at $E = 10^{-6}$, concentrating on Ra values where we expect to be in a regime of nonlinear rotating convection, which is our main region of interest. Gastine *et al.* (2016) produced a regime diagram (their figure 20) showing that the rapidly rotating regime is expected for only a small span of Ra_T for our values of E, being bounded below by the weakly nonlinear regime (when $Ra \leqslant 6Ra_C$) and above by a regime they term transitional, in which rotational effects no longer dominate even if the effectively non-rotating regime has not been reached. Our model has a different aspect ratio, radial gravity profile and thermal boundary conditions than Gastine *et al.* (2016) so an exact correspondence between our results and their regime diagram is not to be expected; however, we observe similar regime transitions.
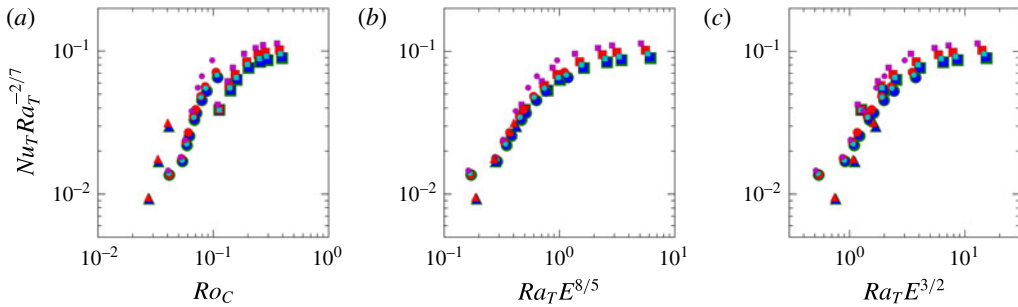
FIGURE 6. (Colour online) Compensated Nusselt number, $NuRa^{-2/7}$, against proposed parameters controlling the transition out of the rotationally dominated regime. For clarity, and to focus on behaviour above the weakly nonlinear regime, only cases with $Ra_F > 7Ra_C$ are shown. (a) $Ro_C = (RaE^2/Pr)^{1/2}$, the convective Rossby number (Gilman 1977). (b) $RaE^{8/5}$, based on the local Rossby number of the thermal boundary layer (Gastine *et al.* 2016). (c) $RaE^{3/2}$, based on thermal and viscous boundary layer crossing (King *et al.* 2012). Symbol shapes indicate the value of E, symbol size and colour indicate the nature of the boundary conditions, as in figure 2.
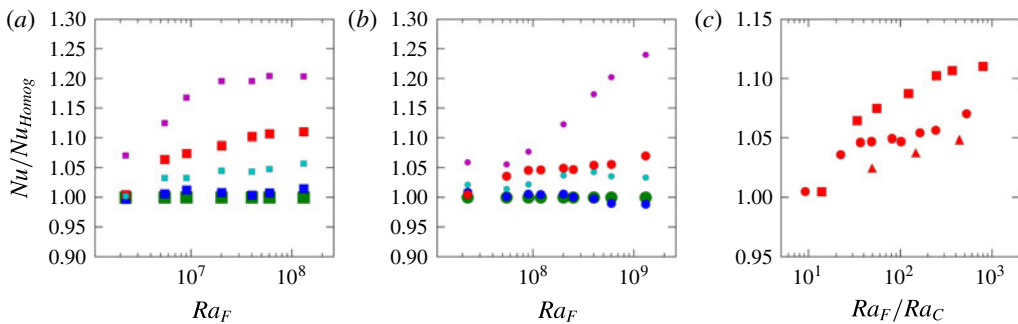
FIGURE 7. (Colour online) Compensated versions of the Nusselt number as a function of Rayleigh number. In each case Nu_T is divided by the value of Nu_T for the homogeneous case at equivalent Ra_F. For clarity, and to focus on behaviour above the weakly nonlinear regime, only cases with $Ra_F > 7Ra_C$ are shown. Symbol colours, shapes and sizes as in figure 5. (a) Runs with $E = 10^{-4}$. (b) Runs with $E = 10^{-5}$. (c) Runs with $Tq_L^\star = 5.0$ plotted as a function of supercriticality.

There is a clear decrease in the slope of the $Nu \propto Ra_T^\gamma$ scaling for the highest Ra_T cases with $E = 10^{-4}$; we do not, however, have sufficient results at high Rayleigh to adequately determine a best-fit scaling. As examples, in figure 5 we plot both $Nu \propto Ra_T^{1/3}$ and $Nu \propto Ra_T^{2/7}$ scalings for comparison with the highest Rayleigh number results with $E = 10^{-4}$. It is unlikely that a single scaling is appropriate over a wide range of Rayleigh number. Previous work in spherical geometry found that continuous changes in flow properties occur within the transitional regime (where our high-Ra_T, $E = 10^{-4}$ results lie), including a reduction in the exponent of the Nu–Ra_T scaling as supercriticality increases and the importance of rotational forces is progressively reduced (Gastine *et al.* 2015, 2016).

The transition from rotationally dominated to non-rotating convection corresponds to buoyancy becoming dominant over Coriolis forces; the most appropriate parameterisation of this transition remains an open question. In figure 6 we plot $NuRa_T^{-2/7}$ against

three proposed transition parameters; to focus on the transition to the non-rotating regime at high Rayleigh number we plot only runs with $Ra_F > 7Ra_C$, which removes cases within the weakly nonlinear regime identified by Gastine *et al.* (2016). The global-scale force balance can be expressed by the convective Rossby number, $Ro_C = (Ra_T E^2/Pr)^{1/2}$, such that the transition to non-rotating convection might be expected when $Ro_C = O(1)$ (Gilman 1977; Zhong *et al.* 2009). We find that all of our runs have $Ro_C < 1$ (figure 6*a*) and do not support a $Ro_C = O(1)$ transition parameter, which agrees with previous numerical and laboratory studies (King *et al.* 2009; Stellmach *et al.* 2014; Cheng *et al.* 2015). Given the importance of the Ekman and thermal boundary layers in controlling heat transport through the system King *et al.* (2012) used the intersection of scaling laws for the thicknesses of these two boundary layers to suggest that the transition should occur for $Ra_T E^{3/2} = O(1)$. If the transition is governed by the loss of geostrophic balance within the thermal boundary layer, scaling of the local Rossby number for the layer leads to a transition occurring at $Ra_T E^{8/5} = O(1)$ (Julien *et al.* 2012*a*; Gastine *et al.* 2016). This latter scaling does a somewhat better job of collapsing our results (compare figure 6*b*,*c*). We would require significantly more high-*Ra* runs to properly characterise both the slope of the *Nu*–*Ra_T* scaling and the transition parameter for the regime in which Coriolis effects no longer dominate buoyancy. Figures 5 and 6 suggests that few (if any) of our $E = 10^{-4}$ runs fall within the nonlinear and rotationally dominated regime, but our runs at lower Ekman do sample this regime, a result consistent with the regime diagram of Gastine *et al.* (2016).

We fit straight lines to each set of four consecutive runs (in terms of their *Ra*) for the $q_L^\star = 0$ simulations at $E = 10^{-4}$ and 10^{-5} and take the line of best fit with maximum slope as the *Nu*–*Ra_T* scaling for the rotating regime. Although all of the runs that end up contributing to this fit may not be rotationally dominated, they are at least rotationally influenced. In both cases the line of steepest slope also corresponds to the four consecutive runs that are best fit by a straight line, although we note that these fits span a limited range of *Ra_T* values. For $E = 10^{-6}$ we fit a straight line to the three $q_L^\star = 0$ simulations. As the Ekman number decreases, the exponent of the *Nu*–*Ra_T* scaling increases from 0.98 for $E = 10^{-4}$, to 1.69 for $E = 10^{-5}$, to 1.86 for $E = 10^{-6}$; such steepening of the *Nu*–*Ra_T* scaling with decreasing *E* has previously been seen in both numerical and laboratory studies of rotating convection in a variety of geometries (e.g. King *et al.* 2012; Cheng *et al.* 2015; Gastine *et al.* 2016). Our scaling is steeper than the diffusivity-free scaling of $Nu \propto Ra_T^{3/2} E^2$ expected at low *E* for convection with free-slip boundaries (Gillet & Jones 2006; Julien *et al.* 2012*a*; Stellmach *et al.* 2014). We employ no-slip boundary conditions for which the effect of Ekman pumping has been shown to increase the efficiency of heat transport and hence the slope of the *Nu*–*Ra_T* scaling (Stellmach *et al.* 2014; Aurnou *et al.* 2015; Julien *et al.* 2016). Although the scaling exponents for our low-*E* runs lie above the diffusivity-free scaling, they are well below the scaling exponents of ~ 3 found in studies with no-slip boundaries in cylindrical and Cartesian geometries at similar *E* (King *et al.* 2012; Cheng *et al.* 2015).

3.3. *Nu enhancement by heterogeneous boundaries*

Our particular interest is whether different boundary heterogeneities alter the amplitude of *Nu* for a given value of *Ra* or even the slope of the associated scaling law; to more clearly show such differences figure 7 presents compensated *Nu* values. In this figure, the *Nu* for each run is divided by the value obtained from the $q_L^\star = 0$ case at the

same Ra_F. There is little difference between the $Tq_L^\star = 2.3$ cases and the equivalent $q_L^\star = 0$ cases. However, in the other cases the heterogeneity in outer boundary heat flux tends to enhance the efficiency of heat transport; the enhancement tends to become greater as Ra becomes more supercritical, the wavelength of the imposed boundary heterogeneity increases, or the amplitude of $q_L^\star$ increases. Investigations of relatively low-Ra convection in high-Pr fluids (Zhang & Gubbins 1993; Davies *et al.* 2009) have found that the effect of outer boundary heterogeneity on the underlying fluid is greater when larger-wavelength lateral variations are applied, consistent with our results at $Pr = 1$ and more highly supercritical Ra.

We find that addition of outer boundary heterogeneity tends to increase Nu relative to equivalent $q_L^\star = 0$ cases, whereas Dietrich *et al.* (2016) found a nearly linear reduction in Nu with increasing $Hq_L^\star$ for simulations with $Ra/Ra_C = 25$, $E = 10^{-4}$ and a range of $0 \leqslant Hq_L^\star \leqslant 2.0$ (see figures 11 and 13 of their paper and note that their definition of $q^\star$ is equal to one half our $Hq_L^\star$). This difference arises from the fact that we use $\overline{\langle \Delta T \rangle}$ in determining Nu_T, whereas Dietrich *et al.* (2016) estimate $\Delta T = T_{max} - T_{min}$, where T_{max} and T_{min} are the maximum and minimum values of T in the domain (Dietrich, personal communication). When there are large lateral variations in boundary heat flux, and hence fluid temperature, the point-wise maximum approach can significantly overestimate the average temperature drop across the system and thus underestimate Nu_T. We have found that calculating $\overline{\langle \Delta T \rangle}$ for their simulations yields an increase in Nu for boundary-forced cases compared to the corresponding homogeneous case.

Differences in the Nusselt number between our $Hq_L^\star = 5.0$ and $q_L^\star = 0$ cases at equivalent Ra_F can be as much as 20–25 % and appear to saturate as the simulations reach the regime where rotation no longer dominates the force balance; this saturation effect is most evident for our $E = 10^{-4}$ cases (figure 7a) as the regime without rotational dominance is more easily reached for larger Ekman number. Since the difference in Nu between the $Hq_L^\star = 5.0$ and $q_L^\star = 0$ cases grows with Ra in the rotationally dominated regime, they are characterised by different exponents for the Nu–Ra_T scaling; for example, we find an exponent of 2.05 for $E = 10^{-5}$ and $Hq_L^\star = 5.0$, significantly above the 1.69 exponent for $q_L^\star = 0$. Although each scaling determination uses only four simulations from a relatively limited range of Ra_T the enhanced efficiency of heat transport in the $Hq_L^\star = 5.0$ cases is clear and much greater than the $Hq_L^\star = 2.3$ cases, which reach at most ~ 5 % enhancement. For the $Tq_L^\star = 5.0$ cases enhancements of about 5 %–10 % are obtained for the three Ekman numbers we consider, with a decrease in the enhancement of Nu as E is lowered (figure 7c). For our lowest E cases we have not been able to reach the regime where rotation no longer dominates the force balance; we expect that the enhancement of the Nusselt number would continue to increase with supercriticality within the rapidly rotating regime, before saturating at sufficiently large Ra_F/Ra_C.

To better understand the Nu enhancement by boundary heterogeneity we consider, as an example, the simulations with $E = 10^{-5}$ and the highest applied Rayleigh number ($Ra_F = 1.3 \times 10^9$). In figure 8 we plot radial profiles of temperature, $\langle \overline{T^\star} \rangle$, advective heat transport, $4\pi r^{\star 2} \langle \overline{u_r^\star T^\star} \rangle$, and diffusive heat transport, $4\pi r^{\star 2} \langle \overline{-\partial T^\star / \partial r^\star} \rangle$. All five cases have thermal boundary layers at the top and bottom of the shell, with the inner boundary layer being more pronounced, and a small but non-zero temperature gradient in the shell interior. For the purposes of plotting $\langle \overline{T^\star} \rangle$ has been set to zero at the inner boundary; differences in $\langle \overline{\Delta T^\star} \rangle$ are thus reflected by the average temperatures plotted at $r_o^\star$. The shape of the temperature profiles for the two $q_L^\star = 5.0$ runs is noticeably different near the top of the shell, with the development of a local maximum in
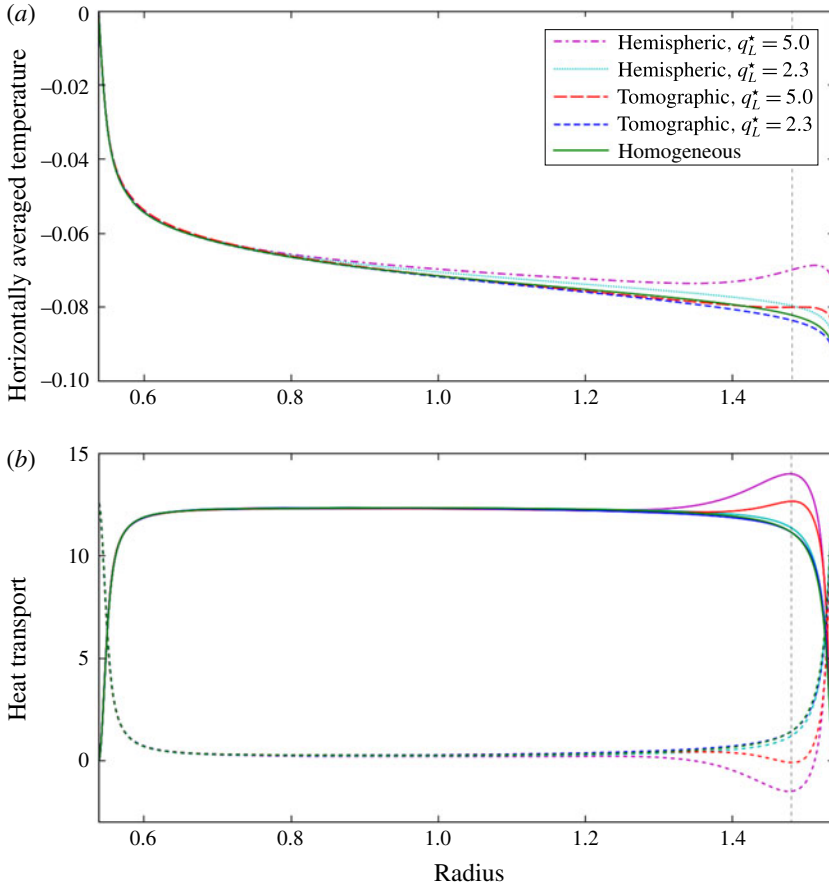
FIGURE 8. (Colour online) (*a*) Radial profiles of $\langle \overline{T^\star} \rangle$ for runs with $E = 10^{-5}$ and $Ra_F = 1.3 \times 10^9$; boundary conditions are indicated by colour and line style. In all cases temperature is set to zero on the inner boundary for the purpose of plotting. (*b*) Profiles of temporally averaged radial heat flow for these runs, solid lines indicate the advective contribution, dashed lines indicate the diffusive contribution; the boundary conditions are indicated by colour as in (*a*). The vertical dashed line indicates the radius for which maps and spectra are plotted in figure 9.

$\langle \overline{T^\star} \rangle$ and hence a region where the radial temperature gradient is positive. There is a corresponding change in the diffusive contribution to the heat transport such that for both of these $q_L^\star = 5.0$ runs there is a depth range near the outer boundary where the net diffusive transport of heat is negative, that is, radially inwards. Since $4\pi r^2 \langle \overline{q} \cdot \hat{r} \rangle$ is conserved, any change in the diffusive contribution is offset by an equal but opposite change in the advective contribution. For the heterogeneous runs shown in figure 8 the modification in heat transport relative to the homogeneous case is constrained to the outer regions of the shell, with larger amplitude and longer-wavelength heterogeneity resulting in changes that extend more deeply.

In figure 9 we plot maps of $\overline{u_r^\star}$ overlain by contours of temperature anomaly, $\overline{T^\star} - \langle \overline{T^\star} \rangle$, as well as the spectra of $(\ell(\ell+1)/(2\ell+1))\overline{p_\ell^m \vartheta_\ell^m}$. In all cases these quantities have been determined for a radius of $r^\star = 1.48$ (the vertical dashed line in figure 8), which lies near the peak in advective heat transport for the $q_L^\star = 5.0$ cases. For the
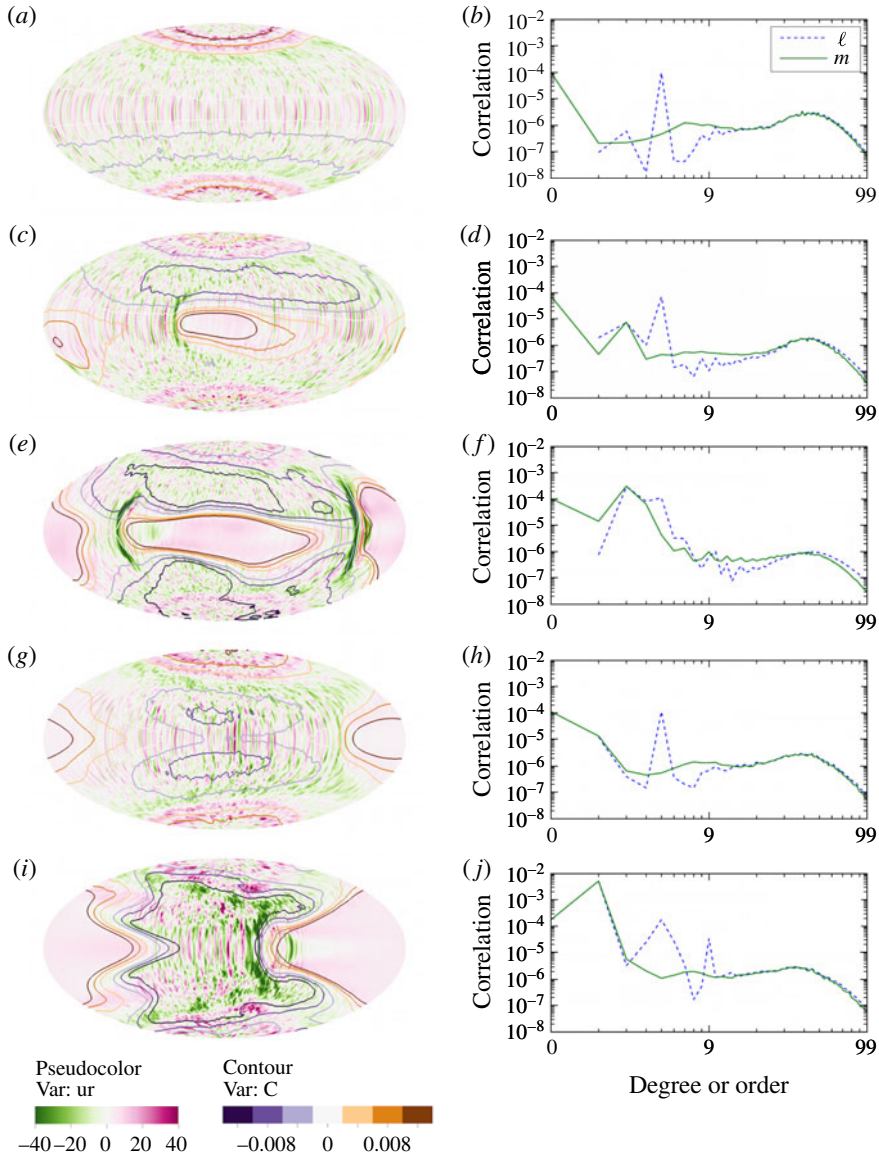
FIGURE 9. (Colour online) Flow and temperature correlations at a radius of $r^\star = 1.48$ for all of the runs with $E = 10^{-5}$ and $Ra_F = 1.3 \times 10^9$; from $(a$–$j)$ the boundary conditions are: $q_L^\star = 0$, $Tq_L^\star = 2.3$, $Tq_L^\star = 5.0$, $Hq_L^\star = 2.3$, $Hq_L^\star = 5.0$. (a,c,e,g,i) Maps of radial velocity (green–magenta) overlain with contours of temperature anomaly (purple–orange); the projection is centred on the negative x-axis, thus q_{max} is centred for the $Hq_L^\star$ cases and one of the q_{min} is approximately centred for the $Tq_L^\star$ cases. (b,d,f,h,j) Spectra of $\overline{u_r^\star T^\star}$; ℓ-spectra (i.e. integration over all m and r for fixed ℓ, dashed blue line), m-spectra (i.e. integration over all ℓ and r for fixed m, solid green line). For the purpose of plotting, spectra are truncated at $\ell = m = 99$.

$q_L^\star = 0$ case the largest single contribution to the advective heat transport comes from the Y_4^0 harmonic; the small-scale convection makes a secondary contribution, with a broad peak in the correlation between $u_r^\star$ and $T^\star$ centred at spherical harmonics of approximately degree and order 40. For this $q_L^\star = 0$ case the polar regions are relatively hot in the time average and temperature anomalies at low to mid-latitudes are weak. For the runs with heterogeneous outer boundaries there is an increased correlation between $u_r^\star$ and $T^\star$ at long wavelengths, with particular enhancement in advective heat transport at spherical harmonics that match the imposed boundary conditions. The contributions identified in the spectra of the homogeneous case are still present, but become relatively less important to the total advective transport as $q_L^\star$ is increased.

For these runs anomalously hot material accumulates near the top of the fluid shell under q_{min}. The formation of small-scale convection rolls is suppressed in these hot regions, with a broad region of relatively weak outward flow favoured instead. The heterogeneous runs also have regions where downwelling is promoted; the time average of the $q_L^\star = 5.0$ runs have regions of particularly intense downwelling near the western edges of the anomalously hot regions. Individual snapshots of the flow show the suppression of small-scale convection under q_{min}; however, the focusing of downwelling is not obvious, emerging only in the time average. The promotion of downwelling at the western boundary of hot regions in these simulations is similar to the jet development observed by Sumita & Olson (1999, 2002) at the front between hot and cold regions in their physical experiment. However, in our numerical simulations the formation of a single spiralling front that spans the shell is prevented by the presence of strong zonal flows of alternating sign in the shell interior. Regardless, the formation of broad regions of weak upwelling and focused regions of enhanced downwelling tends to increase advective heat transport near the top of the shell in these heterogeneous cases and hence raise the Nusselt number relative to the homogeneous case. For the $Tq_L^\star = 2.3$ case there is increased advective transport relative to the homogeneous case at some spherical harmonics, most substantially at Y_2^2; however, these increases do not offset a reduction in the Y_4^0 contribution by $\sim 15\%$. For the $Tq_L^\star = 5.0$ case the reduction in the Y_4^0 contribution relative to $q_L^\star = 0$ is much smaller ($\sim 1\%$) and is more than compensated by increased advective transport at other harmonics. For the $Hq_L^\star = 2.3$ case the Y_4^0 contribution at this radius is increased relative to the homogeneous case by $\sim 10\%$; the relative increase in advective heat transport at Y_1^1 is much larger, but the absolute difference is similar for both harmonics. For the $Hq_L^\star = 5.0$ case the Nusselt number enhancement is dominated by the increased correlation between radial velocity and temperature at Y_1^1. The results in figure 9 are for one particular radius and a single set of simulations, but are representative of the changes seen near the top of the fluid layer when heterogeneous boundary conditions are imposed.

All simulations for which the heterogeneous outer boundary condition increases the Nusselt number must do so by increasing the radial advective transport of heat over some radial extent, which is generally restricted towards the outer regions of the shell in our simulations. There is a corresponding reduction in the diffusive contribution to radial heat transport and thus $\langle \partial T / \partial r \rangle$ becomes less negative in the affected region, relative to the equivalent homogeneous case. In some of our simulations (for example, the $q_L^\star = 5.0$ cases in figure 8) the time-averaged temperature gradient even becomes positive in a region near the outer boundary, an apparent stable stratification.

In principle, our use of the Boussinesq approximation could be invalidated in such cases. The Boussinesq approximation requires that density variation across the system in the background state is sufficiently small (Spiegel & Veronis 1960). Although commonly used in models of planetary cores, this thin layer approximation is only marginally satisfied for Earth's core (see e.g. Jones 2015), which remains true for our investigation. The Boussinesq approximation would also be invalid if the system dynamics produces sufficiently large fluctuations in density (Spiegel & Veronis 1960). Although the time-averaged temperature anomalies in our most extreme heterogeneous cases are large compared to those found in homogeneous convection, the fluctuations at any point in time remain smaller than the static variations of the background state and the Boussinesq approximation still holds.

The large lateral variations in the time-averaged temperature near the top of the shell that arise in these cases are associated with strong variations in local dynamics, with regions of both inhibited and enhanced small-scale convection (figure 9). This situation is in some sense the complement of the physical experiments of Alboussière, Deguen & Melzani (2010) investigating stratification at the bottom of the core due to partial melting of the inner core; they injected fluids that were both compositionally dense and buoyant at the bottom of a tank and found that the upwellings of buoyant fluid did not prevent the formation of a dense, stably stratified layer. We have strong lateral variations in thermal buoyancy generated at the top of the shell; however, the strong localised convection does not preclude the formation of an average stratification, as in the physical experiment. Stratification at the top of Earth's core has been hypothesised based on both seismic and geomagnetic observations, with both thermal and compositional stratification mechanisms proposed (see e.g. Helffrich & Kaneshima 2013). Heterogeneous outer boundary conditions that increase Nu by reorganising flow near the top of the core will necessarily make the average radial temperature gradient more positive in the affected region and can potentially create a thermal stratification signature in the average temperature profile.

4. Conclusions

In planetary settings it is expected that long-wavelength variations in the heat flux at the top of metallic cores beneath convecting silicate mantles will be common, although the pattern and amplitude of these variations are uncertain and will vary both between bodies and through time. We have performed 106 numerical simulations, with three Ekman numbers and five different thermal boundary conditions to investigate how heat transport by thermal convection in rotating spherical shells is impacted by the inclusion of heterogeneous heat flux at the outer boundary. The large amplitude and long-wavelength boundary heterogeneity we considered tends to increase the Nusselt number of the system relative to equivalent homogeneous cases (table 2).

The size of the Nusselt number enhancement tends to increase as the amplitude and wavelength of the boundary heterogeneity increases. The enhancement also tends to increase with the supercriticality of the system, although it may saturate as the system enters the regime in which rotation no longer dominates the force balance. This Rayleigh-dependent enhancement can significantly steepen the $Nu - Ra_T$ scaling within the rotationally dominated regime, particularly for the $q_L^\star = 5.0$ cases. The Nusselt number enhancement arises from an increased correlation between radial flow and temperature, particularly near the top of the shell, due to the development of regions of broad weak upwelling with relatively narrow regions at their western edge where

E	Boundary condition	Nu–Ra_T exponent	Maximum Nu enhancement (%)
10^{-4}	$q_L^\star = 0$	0.98	N/A
10^{-4}	$Tq_L^\star = 2.3$	1.07	1.5
10^{-4}	$Tq_L^\star = 5.0$	1.25	11.1
10^{-4}	$Hq_L^\star = 2.3$	1.02	5.8
10^{-4}	$Hq_L^\star = 5.0$	1.19	20.5
10^{-5}	$q_L^\star = 0$	1.69	N/A
10^{-5}	$Tq_L^\star = 2.3$	1.73	0.9
10^{-5}	$Tq_L^\star = 5.0$	1.80	7.0
10^{-5}	$Hq_L^\star = 2.3$	1.79	4.9
10^{-5}	$Hq_L^\star = 5.0$	2.05	24.1
10^{-6}	$q_L^\star = 0$	1.86	N/A
10^{-6}	$Tq_L^\star = 2.3$	1.85	<0.1
10^{-6}	$Tq_L^\star = 5.0$	1.95	4.9

TABLE 2. Heat transport enhancement results organised by Ekman number and applied boundary condition: exponent of the $Nu \propto Ra_T^\gamma$ scaling in the rotationally dominated regime; and the largest seen enhancement of Nu relative to the equivalent homogeneous Ra_F case.

downwelling is strongly promoted. The fixed-flux boundary conditions require that any increase in the advective contribution to the time-averaged radial heat transport is accompanied by a decrease in the diffusive contribution and hence a modification of the time-averaged temperature profile. In our simulations these effects generally occur near the top of the shell and in some cases can produce an apparent thermal stratification in the time-averaged temperature profile, despite the presence of regions of strong convection at all radii.

Acknowledgements

Appendix A. The non-dimensionalisation of ΔT_C

The temperature drop across the spherical shell with fixed-flux boundary conditions in our pure conduction case is $\Delta T_C = \beta h / r_i r_o$ (2.25). After non-dimensionalisation of length by $h = r_o - r_i$ and temperature by β / h we have

$$\Delta T_C^\star = \frac{1}{r_i^\star r_o^\star}. \tag{A 1}$$

Therefore, when expressed in terms of the non-dimensional temperature we have

$$Nu_{T^\star} = \frac{r_i^\star r_o^\star}{\Delta \langle \overline{T^\star} \rangle}. \tag{A 2}$$

We set our model to match Earth, so $r_i = 1.22 \times 10^6$ m, $r_o = 3.48 \times 10^6$ m and thus $Nu_{T^\star} \approx 1.2/\Delta \langle \overline{T^\star} \rangle$. We highlight this result in contrast to the plane layer geometry for which $Nu_{T^\star} = 1/\Delta \langle \overline{T^\star} \rangle$ (e.g. Otero *et al.* 2002).

Since our temperature scaling depends on shell geometry, it is possible to construct a spherical shell for which $Nu_{T^\star} = 1$ as in the plane layer case. The combination of temperature and length non-dimensionalisation would then imply

$$1 = \frac{1}{r_i^\star r_o^\star}, \tag{A 3}$$

$$1 = r_o^\star - r_i^\star. \tag{A 4}$$

The solution is

$$r_i^\star = \frac{\sqrt{5}}{2} - \frac{1}{2} = \frac{1}{\varphi}, \tag{A 5}$$

$$r_o^\star = \frac{\sqrt{5}}{2} + \frac{1}{2} = \varphi, \tag{A 6}$$

giving a radius ratio $r_i/r_o = 1/\varphi^2 \approx 0.382$, not far from the value of ~ 0.351 for Earth.

Appendix B. Tables of results

Summary tables of the model resolution, control parameters and selected output parameters for all simulations. In all cases $Pr = 1$ and the radius ratio $r_i/r_o = 0.351$. N_r is the number of radial points within the fluid shell. $N_{\delta i}$ and $N_{\delta o}$ are the number of radial points within the mechanical boundary layer at the inner and outer boundary, respectively. $\ell_{max} = m_{max}$ is the maximum degree and order of spherical harmonic expansion. Definitions of the Ekman number and modified Rayleigh number are given in (2.10). The amplitude of the heterogeneity in outer boundary heat flux is defined in (1.1); $q_L^\star = 0$ are homogeneous cases, $Tq_L^\star$ are cases with a pattern of heat flux derived from mantle tomography, $Hq_L^\star$ are cases with a hemispheric (Y_1^1) pattern. Nu_T is given by (2.30). The Reynolds number is determined by (2.16) and hence the kinetic energy integral (2.17). Re_{pol} is found by retaining only the poloidal component of velocity (recall (2.4)) in the kinetic energy integral. Re_{zon} is found by retaining only the $m = 0$ components from the spherical harmonic expansion of the toroidal component of velocity in the kinetic energy integral. P is the time average of the buoyancy production throughout the shell, ϵ_U is the time average of the viscous dissipation throughout the shell.

Boundary	$\widetilde{Ra}$	Nu_T	Re	Re_{pol}	Re_{zon}	P	ϵ_U	N_r	ℓ_{max}	$N_{\delta i}$	$N_{\delta o}$
$q_L^\star = 0$	30	1.19	15.0	5.7	2.2	4.78021×10^5	4.78022×10^5	64	48	10	26
$q_L^\star = 0$	90	1.62	38.8	14.9	13.9	4.09815×10^6	4.10101×10^6	64	64	10	10
$q_L^\star = 0$	100	1.71	40.4	15.8	14.0	4.24413×10^6	4.25138×10^6	60	48	9	19
$q_L^\star = 0$	150	1.89	50.1	21.5	17.0	7.52380×10^6	7.54178×10^6	80	64	12	12
$q_L^\star = 0$	225	2.16	64.0	29.5	21.7	1.58309×10^7	1.58508×10^7	80	92	12	11
$q_L^\star = 0$	550	3.36	96.9	51.6	27.2	5.10257×10^7	5.10242×10^7	80	92	10	11
$q_L^\star = 0$	900	4.27	124.3	68.8	36.0	9.23021×10^7	9.23000×10^7	80	92	9	10
$q_L^\star = 0$	2 000	5.92	193.4	107.1	70.2	2.24262×10^8	2.24184×10^8	96	96	12	13
$q_L^\star = 0$	4 000	7.44	276.3	152.9	113.4	4.67205×10^8	4.66904×10^8	96	96	12	13
$q_L^\star = 0$	6 000	8.35	332.8	189.0	129.4	7.08226×10^8	7.08971×10^8	128	128	15	18
$q_L^\star = 0$	13 000	10.16	483.1	273.3	215.0	1.56626×10^9	1.56477×10^9	128	128	16	18
$Tq_L^\star = 2.3$	30	1.18	14.6	5.5	3.0	4.53139×10^5	4.53161×10^5	64	64	10	25
$Tq_L^\star = 2.3$	90	1.56	36.2	14.0	14.7	3.79416×10^6	3.79750×10^6	64	64	10	10
$Tq_L^\star = 2.3$	225	2.15	61.7	28.6	23.3	1.58478×10^7	1.58566×10^7	80	92	12	11
$Tq_L^\star = 2.3$	550	3.38	93.3	50.7	29.3	5.11910×10^7	5.12066×10^7	80	92	10	10
$Tq_L^\star = 2.3$	900	4.33	125.3	68.8	33.6	9.28297×10^7	9.28697×10^7	80	92	10	10
$Tq_L^\star = 2.3$	2 000	5.97	190.3	107.6	49.9	2.24701×10^8	2.24704×10^8	96	96	12	13
$Tq_L^\star = 2.3$	4 000	7.47	265.7	153.9	78.0	4.66833×10^8	4.66660×10^8	96	96	12	13
$Tq_L^\star = 2.3$	6 000	8.41	322.3	186.7	107.3	7.11691×10^8	7.11134×10^8	128	128	15	17
$Tq_L^\star = 2.3$	13 000	10.32	459.7	276.4	132.8	1.57402×10^9	1.57212×10^9	128	128	15	18
$Tq_L^\star = 5.0$	30	1.20	16.0	5.9	4.0	4.88902×10^5	4.88902×10^5	64	64	10	24
$Tq_L^\star = 5.0$	90	1.56	37.2	13.8	17.1	4.08174×10^6	4.08853×10^6	64	64	19	10
$Tq_L^\star = 5.0$	225	2.16	57.3	28.0	25.3	1.61914×10^7	1.61994×10^7	80	92	10	11
$Tq_L^\star = 5.0$	550	3.57	93.8	50.8	33.4	5.40076×10^7	5.40223×10^7	80	92	10	10
$Tq_L^\star = 5.0$	900	4.59	121.9	68.3	38.7	9.67341×10^7	9.67580×10^7	80	92	10	10
$Tq_L^\star = 5.0$	2 000	6.43	184.8	106.3	54.7	2.33029×10^8	2.33003×10^8	96	96	12	13
$Tq_L^\star = 5.0$	4 000	8.21	261.0	153.7	67.4	4.83518×10^8	4.83796×10^8	96	96	12	13
$Tq_L^\star = 5.0$	6 000	9.24	316.8	188.8	82.2	7.33091×10^8	7.33801×10^8	128	128	15	17
$Tq_L^\star = 5.0$	13 000	11.28	456.5	275.5	122.9	1.60985×10^9	1.61080×10^9	128	128	15	18
$Hq_L^\star = 2.3$	30	1.19	13.8	5.9	1.5	4.77130×10^5	4.77107×10^5	64	48	10	10
$Hq_L^\star = 2.3$	90	1.66	40.3	16.0	14.0	4.70090×10^6	4.70703×10^6	64	64	10	10
$Hq_L^\star = 2.3$	225	2.17	62.8	29.5	22.9	1.61102×10^7	1.61326×10^7	80	92	12	11
$Hq_L^\star = 2.3$	550	3.47	103.0	52.6	32.7	5.24670×10^7	5.25358×10^7	80	92	10	11
$Hq_L^\star = 2.3$	900	4.41	134.5	70.5	42.7	9.39105×10^7	9.39404×10^7	80	92	10	11
$Hq_L^\star = 2.3$	2 000	6.20	204.9	110.1	66.0	2.27285×10^8	2.27356×10^8	96	96	12	13
$Hq_L^\star = 2.3$	4 000	7.78	287.5	157.9	98.2	4.69832×10^8	4.70235×10^8	96	96	12	13
$Hq_L^\star = 2.3$	6 000	8.76	348.5	194.7	118.2	7.15230×10^8	7.15039×10^8	128	128	16	18
$Hq_L^\star = 2.3$	13 000	10.76	502.3	283.2	169.8	1.58059×10^9	1.57940×10^9	128	128	16	18
$Hq_L^\star = 5.0$	30	1.42	22.5	8.8	5.7	1.30797×10^6	1.30797×10^6	64	48	10	17
$Hq_L^\star = 5.0$	90	1.73	42.7	17.1	16.6	5.64898×10^6	5.66254×10^6	64	64	10	10
$Hq_L^\star = 5.0$	225	2.33	67.3	31.5	26.0	1.86103×10^7	1.86548×10^7	80	92	12	11
$Hq_L^\star = 5.0$	550	3.78	106.7	55.2	37.0	5.75056×10^7	5.75666×10^7	80	92	10	11
$Hq_L^\star = 5.0$	900	5.00	141.3	74.0	46.0	1.02083×10^8	1.02217×10^8	80	92	10	11
$Hq_L^\star = 5.0$	2 000	7.10	211.8	114.0	67.6	2.41234×10^8	2.41658×10^8	96	96	12	13
$Hq_L^\star = 5.0$	4 000	8.92	296.3	162.3	102.9	4.94373×10^8	4.94661×10^8	128	128	16	19
$Hq_L^\star = 5.0$	6 000	10.07	359.5	197.8	130.4	7.48688×10^8	7.49483×10^8	128	128	16	19
$Hq_L^\star = 5.0$	13 000	12.25	509.5	286.1	187.4	1.64536×10^9	1.64421×10^9	128	128	16	20

TABLE 3. Summary of all runs for $E = 10^{-4}$.

Boundary	$\widetilde{Ra}$	Nu_T	Re	Re_{pol}	Re_{zon}	P	ϵ_U	N_r	ℓ_{max}	$N_{\delta i}$	$N_{\delta o}$
$q_L^\star = 0$	30	1.03	7.1	3.4	0.7	4.30198×10^5	4.30198×10^5	80	64	28	5
$q_L^\star = 0$	90	1.25	38.5	16.5	14.5	1.34837×10^7	1.34839×10^7	90	80	22	7
$q_L^\star = 0$	150	1.43	65.7	27.0	21.6	3.98206×10^7	3.98214×10^7	90	80	22	8
$q_L^\star = 0$	225	1.58	86.2	35.3	34.1	8.12987×10^7	8.13030×10^7	90	128	9	7
$q_L^\star = 0$	550	2.29	150.2	71.8	51.1	3.74397×10^8	3.74562×10^8	90	128	7	8
$q_L^\star = 0$	900	3.13	199.0	101.2	62.9	7.58361×10^8	7.58773×10^8	90	128	7	8
$q_L^\star = 0$	1 200	3.75	234.2	121.7	69.3	1.09936×10^9	1.09929×10^9	90	128	7	8
$q_L^\star = 0$	2 000	5.14	316.1	167.4	95.0	2.06032×10^9	2.06007×10^9	128	144	9	10
$q_L^\star = 0$	2 500	5.88	361.2	190.4	121.1	2.67403×10^9	2.67356×10^9	128	144	9	10
$q_L^\star = 0$	4 000	7.67	472.3	249.8	170.4	4.52798×10^9	4.52712×10^9	192	192	14	14
$q_L^\star = 0$	6 000	9.47	598.3	310.3	259.7	7.02322×10^9	7.02222×10^9	192	192	14	14
$q_L^\star = 0$	13 000	13.29	927.8	456.6	512.4	1.58024×10^{10}	1.57922×10^{10}	256	256	16	14
$Tq_L^\star = 2.3$	30	1.02	6.5	2.8	2.3	3.64894×10^5	3.64895×10^5	128	96	28	7
$Tq_L^\star = 2.3$	90	1.24	38.3	15.7	15.1	1.26866×10^7	1.26866×10^7	128	96	33	10
$Tq_L^\star = 2.3$	225	1.60	89.4	36.3	34.5	8.45382×10^7	8.45432×10^7	128	96	33	10
$Tq_L^\star = 2.3$	550	2.30	146.4	70.6	52.2	3.75773×10^8	3.75913×10^8	90	128	7	8
$Tq_L^\star = 2.3$	900	3.14	195.0	99.4	62.7	7.62351×10^8	7.62548×10^8	90	128	7	8
$Tq_L^\star = 2.3$	1 200	3.77	229.3	120.1	69.7	1.10618×10^9	1.10655×10^9	90	128	7	8
$Tq_L^\star = 2.3$	2 000	5.17	310.2	164.3	94.4	2.06876×10^9	2.06925×10^9	128	144	9	10
$Tq_L^\star = 2.3$	2 500	5.89	351.1	187.0	110.2	2.68093×10^9	2.68059×10^9	128	144	9	10
$Tq_L^\star = 2.3$	4 000	7.65	456.4	244.0	161.8	4.52501×10^9	4.52599×10^9	192	192	14	14
$Tq_L^\star = 2.3$	6 000	9.37	564.1	305.0	201.2	7.01606×10^9	7.01647×10^9	192	192	14	14
$Tq_L^\star = 2.3$	13 000	13.13	861.3	452.2	402.3	1.57709×10^{10}	1.57698×10^{10}	192	192	14	14
$Tq_L^\star = 5.0$	30	1.01	7.9	2.6	4.3	4.87080×10^5	4.87079×10^5	128	96	52	12
$Tq_L^\star = 5.0$	90	1.27	41.6	16.9	13.5	1.48061×10^7	1.48063×10^7	90	96	23	16
$Tq_L^\star = 5.0$	225	1.59	90.1	35.4	38.6	8.71763×10^7	8.72294×10^7	128	96	31	10
$Tq_L^\star = 5.0$	550	2.38	145.6	69.9	59.7	3.95231×10^8	3.95306×10^8	90	128	7	8
$Tq_L^\star = 5.0$	900	3.27	190.3	98.4	66.7	7.96897×10^8	7.97092×10^8	90	128	7	8
$Tq_L^\star = 5.0$	1 200	3.92	223.2	118.0	73.5	1.15361×10^9	1.15369×10^9	90	128	7	8
$Tq_L^\star = 5.0$	2 000	5.39	296.0	160.7	91.5	2.13375×10^9	2.13370×10^9	128	144	9	10
$Tq_L^\star = 5.0$	2 500	6.16	336.6	183.8	101.5	2.76352×10^9	2.76337×10^9	128	144	9	10
$Tq_L^\star = 5.0$	4 000	8.08	433.5	240.8	129.5	4.65028×10^9	4.65196×10^9	192	192	14	14
$Tq_L^\star = 5.0$	6 000	10.00	540.7	300.1	179.4	7.19371×10^9	7.19458×10^9	192	192	14	14
$Tq_L^\star = 5.0$	13 000	14.22	812.1	446.4	327.4	1.61015×10^{10}	1.61076×10^{10}	192	192	14	14
$Hq_L^\star = 2.3$	30	1.04	10.7	4.7	1.1	1.04198×10^6	1.04198×10^6	80	64	34	12
$Hq_L^\star = 2.3$	90	1.31	44.6	19.4	12.5	1.90383×10^7	1.90388×10^7	90	80	34	8
$Hq_L^\star = 2.3$	225	1.62	91.8	38.0	33.3	9.29168×10^7	9.30683×10^7	90	128	23	8
$Hq_L^\star = 2.3$	550	2.33	154.5	73.7	53.5	3.90540×10^8	3.90853×10^8	90	128	7	8
$Hq_L^\star = 2.3$	900	3.19	205.7	103.3	66.7	7.80866×10^8	7.81356×10^8	90	128	7	8
$Hq_L^\star = 2.3$	2 000	5.33	332.3	170.9	103.1	2.11004×10^9	2.11030×10^9	128	144	10	10
$Hq_L^\star = 2.3$	4 000	8.00	493.1	253.9	191.6	4.59532×10^9	4.59673×10^9	192	192	14	14
$Hq_L^\star = 2.3$	6 000	9.81	616.3	315.6	269.7	7.10168×10^9	7.10107×10^9	192	192	14	14
$Hq_L^\star = 2.3$	13 000	13.74	938.2	466.5	492.8	1.59043×10^{10}	1.59169×10^{10}	256	256	20	20
$Hq_L^\star = 5.0$	30	1.08	17.1	7.2	2.0	2.86108×10^6	2.86107×10^6	80	64	36	7
$Hq_L^\star = 5.0$	90	1.48	62.8	25.7	22.8	4.47602×10^7	4.47520×10^7	96	96	25	10
$Hq_L^\star = 5.0$	225	1.68	97.8	40.8	36.9	1.12445×10^8	1.12655×10^8	90	128	24	8
$Hq_L^\star = 5.0$	550	2.42	160.5	77.1	59.5	4.29394×10^8	4.29842×10^8	90	128	7	8
$Hq_L^\star = 5.0$	900	3.37	213.5	107.3	72.5	8.41615×10^8	8.42580×10^8	90	128	7	8
$Hq_L^\star = 5.0$	2 000	5.77	339.3	175.2	101.6	2.22759×10^9	2.23006×10^9	128	144	10	10
$Hq_L^\star = 5.0$	4 000	9.01	498.5	259.7	173.8	4.84436×10^9	4.85116×10^9	192	192	14	15
$Hq_L^\star = 5.0$	6 000	11.39	622.6	321.5	246.0	7.45281×10^9	7.46115×10^9	192	192	14	15
$Hq_L^\star = 5.0$	13 000	16.49	958.4	488.9	437.4	1.69246×10^{10}	1.70334×10^{10}	256	256	21	20

TABLE 4. Summary of all runs with $E = 10^{-5}$.

Boundary	$\widetilde{Ra}$	Nu_T	Re	Re_{pol}	Re_{zon}	P	ϵ_U	N_r	ℓ_{max}	$N_{\delta i}$	$N_{\delta o}$
$q_L^\star = 0$	2 000	3.19	504.1	251.6	139.0	1.61586×10^{10}	1.61648×10^{10}	192	192	11	10
$q_L^\star = 0$	6 000	6.51	951.9	488.2	308.6	6.00882×10^{10}	6.02028×10^{10}	224	224	12	12
$q_L^\star = 0$	18 000	12.92	1670.0	849.7	689.4	1.70352×10^{11}	1.71287×10^{11}	320	320	16	15
$Tq_L^\star = 2.3$	2 000	3.19	489.6	245.7	140.2	1.62591×10^{10}	1.62616×10^{10}	192	192	11	10
$Tq_L^\star = 2.3$	6 000	6.50	926.9	482.1	282.8	6.28045×10^{10}	6.28064×10^{10}	224	224	12	12
$Tq_L^\star = 2.3$	18 000	12.87	1768.5	893.8	790.8	2.10229×10^{11}	2.10222×10^{11}	320	320	16	15
$Tq_L^\star = 5.0$	2 000	3.26	478.2	241.7	146.7	1.68536×10^{10}	1.68587×10^{10}	192	192	11	10
$Tq_L^\star = 5.0$	6 000	6.75	881.6	460.8	274.3	6.07211×10^{10}	6.08708×10^{10}	224	224	11	12
$Tq_L^\star = 5.0$	18 000	13.55	1698.9	873.6	693.6	2.08698×10^{11}	2.07256×10^{11}	320	320	16	15

TABLE 5. Summary of all runs with $E = 10^{-6}$.

REFERENCES

AHLERS, G., GROSSMANN, S. & LOHSE, D. 2009 Heat transfer and large scale dynamics in turbulent Rayleigh–Bénard convection. *Rev. Mod. Phys.* **81** (2), 503–537.

ALBOUSSIÈRE, T., DEGUEN, R. & MELZANI, M. 2010 Melting-induced stratification above the Earth's inner core due to convective translation. *Nature* **466** (7307), 744–747.

AMIT, H., AUBERT, J. & HULOT, G. 2010 Stationary, oscillating or drifting mantle-driven geomagnetic flux patches? *J. Geophys. Res.* **115** (B7), B07108.

AMIT, H., CHOBLET, G., OLSON, P., MONTEUX, J., DESCHAMPS, F., LANGLAIS, B. & TOBIE, G. 2015a Towards more realistic core–mantle boundary heat flux patterns: a source of diversity in planetary dynamos. *Prog. Earth Planetary Sci.* **2**, 26.

AMIT, H., DESCHAMPS, F. & CHOBLET, G. 2015b Numerical dynamos with outer boundary heat flux inferred from probabilistic tomography – consequences for latitudinal distribution of magnetic flux. *Geophys. J. Intl* **203**, 840–855.

AURNOU, J. M., CALKINS, M. A., CHENG, J. S., JULIEN, K., KING, E. M., NIEVES, D., SODERLUND, K. M. & STELLMACH, S. 2015 Rotating convective turbulence in Earth and planetary cores. *Phys. Earth Planet. Inter.* **246**, 52–71.

BLOXHAM, J. 2000 The effect of thermal core–mantle interactions on the palaeomagnetic secular variation. *Phil. Trans. R. Soc. Lond.* A **358** (1768), 1171–1179.

BUSSE, F. H. 2002 Convective flows in rapidly rotating spheres and their dynamo action. *Phys. Fluids* **14** (4), 1301–1314.

CALKINS, M. A., HALE, K., JULIEN, K., NIEVES, D., DRIGGS, D. & MARTI, P. 2015 The asymptotic equivalence of fixed heat flux and fixed temperature thermal boundary conditions for rapidly rotating convection. *J. Fluid Mech.* **784**, R2.

CHENG, J. S., STELLMACH, S., RIBEIRO, A., GRANNAN, A., KING, E. M. & AURNOU, J. M. 2015 Laboratory-numerical models of rapidly rotating convection in planetary cores. *Geophys. J. Intl* **201**, 1–17.

CHILDS, H., BRUGGER, E., WHITLOCK, B., MEREDITH, J., AHERN, S., PUGMIRE, D., BIAGAS, K., MILLER, M., HARRISON, C., WEBER, G. H. *et al.* 2012 VisIt: an end-user tool for visualizing and analyzing very large data. In *High Performance Visualization* (ed. E. Wes Bethel, H. Childs & C. Hansen), pp. 357–372. Chapman and Hall.

DAVIES, C. J. 2015 Cooling history of Earth's core with high thermal conductivity. *Phys. Earth Planet. Inter.* **247**, 65–79.

DAVIES, C. J., GUBBINS, D. & JIMACK, P. K. 2009 Convection in a rapidly rotating spherical shell with an imposed laterally varying thermal boundary condition. *J. Fluid Mech.* **641**, 335–358.

DAVIES, C. J., GUBBINS, D., WILLIS, A. P. & JIMACK, P. K. 2008 Time-averaged paleomagnetic field and secular variation: predictions from dynamo solutions based on lower mantle seismic tomography. *Phys. Earth Planet. Inter.* **169** (1–4), 194–203.

DIETRICH, W., HORI, K. & WICHT, J. 2016 Core flows and heat transfer induced by inhomogeneous cooling with sub- and supercritical convection. *Phys. Earth Planet. Inter.* **251**, 36–51.

GARNERO, E. J., MCNAMARA, A. K. & SHIM, S.-H. 2016 Continent-sized anomalous zones with low seismic velocity at the base of Earth's mantle. *Nat. Geosci.* **9** (7), 481–489.

GASTINE, T., WICHT, J. & AUBERT, J. 2016 Scaling regimes in spherical shell rotating convection. *J. Fluid Mech.* **808**, 690–732.

GASTINE, T., WICHT, J. & AURNOU, J. M. 2015 Turbulent Rayleigh–Bénard convection in spherical shells. *J. Fluid Mech.* **778**, 721–764.

GELMAN, S. E., ELKINS-TANTON, L. T. & SEAGER, S. 2011 Effects of stellar flux on tidally locked terrestrial planets: degree-1 mantle convection and local magma ponds. *Astrophys. J.* **735** (2), 72.

GIBBONS, S. J., GUBBINS, D. & ZHANG, K. 2007 Convection in rotating spherical fluid shells with inhomogeneous heat flux at the outer boundary. *Geophys. Astrophys. Fluid Dyn.* **101** (5–6), 347–370.

GILLET, N. & JONES, C. A. 2006 The quasi-geostrophic model for rapidly rotating spherical convection outside the tangent cylinder. *J. Fluid Mech.* **554**, 343–369.

GILMAN, P. A. 1977 Nonlinear dynamics of Boussinesq convection in a deep rotating spherical shell-i. *Geophys. Astrophys. Fluid Dyn.* **8** (1), 93–135.

GOLUSKIN, D. 2015 *Internally Heated Convection and Rayleigh–Bénard Convection*. Springer.

GROSSMANN, S. & LOHSE, D. 2000 Scaling in thermal convection: a unifying theory. *J. Fluid Mech.* **407**, 27–56.

GROSSMANN, S. & LOHSE, D. 2001 Thermal convection for large Prandtl numbers. *Phys. Rev. Lett.* **86** (15), 3316–3319.

GROSSMANN, S. & LOHSE, D. 2002 Prandtl and Rayleigh number dependence of the Reynolds number in turbulent thermal convection. *Phys. Rev.* E **66** (1), 016305.

GUBBINS, D., WILLIS, A. P. & SREENIVASAN, B. 2007 Correlation of Earth's magnetic field with lower mantle thermal and seismic structure. *Phys. Earth Planet. Inter.* **162** (3–4), 256–260.

HELFFRICH, G. & KANESHIMA, S. 2013 Causes and consequences of outer core stratification. *Phys. Earth Planet. Inter.* **223** (C), 2–7.

HUNTER, J. D. 2007 Matplotlib: a 2D graphics environment. *Comput. Sci. Engng* **9** (3), 90–95.

JOHNSTON, H. & DOERING, C. R. 2009 Comparison of turbulent thermal convection between conditions of constant temperature and constant flux. *Phys. Rev. Lett.* **102** (6), 064501.

JONES, C. A. 2015 Thermal and compositional convection in the outer core. In *Treatise on Geophysics*, 2nd edn (ed. G. Schubert), vol. 8, pp. 115–159. Elsevier.

JULIEN, K., AURNOU, J. M., CALKINS, M. A., KNOBLOCH, E., MARTI, P., STELLMACH, S. & VASIL, G. M. 2016 A nonlinear model for rotationally constrained convection with Ekman pumping. *J. Fluid Mech.* **798**, 50–87.

JULIEN, K., KNOBLOCH, E., RUBIO, A. M. & VASIL, G. M. 2012*a* Heat transport in low-Rossby-number Rayleigh–Bénard convection. *Phys. Rev. Lett.* **109** (25), 254503.

JULIEN, K., RUBIO, A. M., GROOMS, I. & KNOBLOCH, E. 2012*b* Statistical and physical balances in low Rossby number Rayleigh–Bénard convection. *Geophys. Astrophys. Fluid Dyn.* **106** (4–5), 392–428.

KAVNER, A. & RAINEY, E. S. G. 2016 Heat transfer in the core and mantle. In *Deep Earth Physics and Chemistry of the Lower Mantle and Core, Geophysical Monograph Series* (ed. H. Terasaki & R. A. Fischer), pp. 31–42. Wiley.

KING, E. M., STELLMACH, S. & AURNOU, J. M. 2012 Heat transfer by rapidly rotating Rayleigh–Bénard convection. *J. Fluid Mech.* **691**, 568–582.

KING, E. M., STELLMACH, S. & BUFFETT, B. 2013 Scaling behaviour in Rayleigh–Bénard convection with and without rotation. *J. Fluid Mech.* **717**, 449–471.

KING, E. M., STELLMACH, S., NOIR, J., HANSEN, U. & AURNOU, J. M. 2009 Boundary layer control of rotating convection systems. *Nature* **457** (7227), 301–304.

KONO, M. 2015 Geomagnetism: an introduction and overview. In *Treatise on Geophysics*, 2nd edn (ed. G. Schubert), vol. 5, pp. 1–31. Elsevier.

LAY, T., HERNLUND, J. & BUFFETT, B. A. 2008 Core–mantle boundary heat flow. *Nat. Geosci.* **1** (1), 25–32.

MALKUS, W. V. R. 1954 The heat transport and spectrum of thermal turbulence. *Proc. R. Soc. Lond.* A **225** (1161), 196–212.

MASTERS, G., JOHNSON, S., LASKE, G. & BOLTON, H. 1996 A shear-velocity model of the mantle. *Phil. Trans. R. Soc. Lond.* A **354** (1711), 1385–1411.

MATSUI, H., HEIEN, E., AUBERT, J., AURNOU, J. M., AVERY, M., BROWN, B., BUFFETT, B. A., BUSSE, F., CHRISTENSEN, U. R., DAVIES, C. J. *et al.* 2016 Performance benchmarks for a next generation numerical dynamo model. *Geochem. Geophys. Geosyst.* **17** (5), 1586–1607.

NAKAGAWA, T. & TACKLEY, P. J. 2008 Lateral variations in CMB heat flux and deep mantle seismic velocity caused by a thermal–chemical-phase boundary layer in 3D spherical convection. *Earth Planet. Sci. Lett.* **271** (1–4), 348–358.

NIMMO, F. 2015 Thermal and compositional evolution of the core. In *Treatise on Geophysics*, 2nd edn (ed. G. Schubert), vol. 9, pp. 201–219. Elsevier.

OLIVEIRA, J. S. & WIECZOREK, M. A. 2017 Testing the axial dipole hypothesis for the Moon by modeling the direction of crustal magnetization. *J. Geophys. Res.* **122** (2), 383–399.

OLSON, P. 2003 Thermal interaction of the core and mantle. In *Earth's Core and Lower Mantle*, pp. 1–38. Taylor & Francis.

OLSON, P. 2016 Mantle control of the geodynamo: consequences of top–down regulation. *Geochem. Geophys. Geosyst.* **17** (5), 1935–1956.

OLSON, P. & CHRISTENSEN, U. R. 2002 The time-averaged magnetic field in numerical dynamos with non-uniform boundary heat flow. *Geophys. J. Intl* **151** (3), 809–823.

OLSON, P., DEGUEN, R., HINNOV, L. A. & ZHONG, S. 2013 Controls on geomagnetic reversals and core evolution by mantle convection in the Phanerozoic. *Phys. Earth Planet. Inter.* **214** (C), 87–103.

OLSON, P., DEGUEN, R., RUDOLPH, M. L. & ZHONG, S. 2015 Core evolution driven by mantle global circulation. *Phys. Earth Planet. Inter.* **243** (C), 44–55.

ORSZAG, S. A. 1971 Numerical simulation of incompressible flows within simple boundaries. I. Galerkin (spectral) representations. *Stud. Appl. Maths* **50** (4), 293–327.

OTERO, J., WITTENBERG, R. W., WORTHING, R. A. & DOERING, C. R. 2002 Bounds on Rayleigh–Bénard convection with an imposed heat flux. *J. Fluid Mech.* **473**, 191–199.

PLUMLEY, M., JULIEN, K., MARTI, P. & STELLMACH, S. 2016 The effects of Ekman pumping on quasi-geostrophic Rayleigh–Bénard convection. *J. Fluid Mech.* **803**, 51–71.

SPIEGEL, E. A. & VERONIS, G. 1960 On the Boussinesq approximation for a compressible fluid. *Astrophys. J.* **131**, 442–447.

SPRAGUE, M., JULIEN, K., KNOBLOCH, E. & WERNE, J. 2006 Numerical simulation of an asymptotically reduced system for rotationally constrained convection. *J. Fluid Mech.* **551**, 141–174.

ŠRÁMEK, O. & ZHONG, S. 2010 Long-wavelength stagnant lid convection with hemispheric variation in lithospheric thickness: link between Martian crustal dichotomy and Tharsis? *J. Geophys. Res.* **115** (E9), E09010.

STELLMACH, S., LISCHPER, M., JULIEN, K., VASIL, G., CHENG, J. S., RIBEIRO, A., KING, E. M. & AURNOU, J. M. 2014 Approaching the asymptotic regime of rapidly rotating convection: boundary layers versus interior dynamics. *Phys. Rev. Lett.* **113** (25), 254501.

STEVENS, R. J. A. M., VAN DER POEL, E. P., GROSSMANN, S. & LOHSE, D. 2013 The unifying theory of scaling in thermal convection: the updated prefactors. *J. Fluid Mech.* **730**, 295–308.

STEVENS, R. J. A. M., VERZICCO, R. & LOHSE, D. 2010 Radial boundary layer structure and Nusselt number in Rayleigh–Bénard convection. *J. Fluid Mech.* **643**, 495–507.

SUMITA, I. & OLSON, P. 1999 A laboratory model for convection in Earth's core driven by a thermally heterogeneous mantle. *Science* **286** (5444), 1547–1549.

SUMITA, I. & OLSON, P. 2002 Rotating thermal convection experiments in a hemispherical shell with heterogeneous boundary heat flux: implications for the Earth's core. *J. Geophys. Res.* **107** (B8), 2169.

TAKAHASHI, F. & TSUNAKAWA, H. 2009 Thermal core–mantle coupling in an early lunar dynamo: implications for a global magnetic field and magnetosphere of the early Moon. *Geophys. Res. Lett.* **36** (24), L24202.

WILLIS, A. P., SREENIVASAN, B. & GUBBINS, D. 2007 Thermal core–mantle interaction: exploring regimes for 'locked' dynamo action. *Phys. Earth Planet. Inter.* **165** (1–2), 83–92.

ZHANG, K. & GUBBINS, D. 1993 Convection in a rotating spherical fluid shell with an inhomogeneous temperature boundary condition at infinite Prandtl number. *J. Fluid Mech.* **250**, 209–232.

ZHANG, K. & GUBBINS, D. 1996 Convection in a rotating spherical fluid shell with an inhomogeneous temperature boundary condition at finite Prandtl number. *Phys. Fluids* **8** (5), 1141–1148.

ZHANG, N. & ZHONG, S. 2011 Heat fluxes at the Earth's surface and core–mantle boundary since Pangea formation and their implications for the geomagnetic superchrons. *Earth Planet. Sci. Lett.* **306** (3–4), 205–216.

ZHONG, J.-Q., STEVENS, R. J. A. M., CLERCX, H. J. H., VERZICCO, R., LOHSE, D. & AHLERS, G. 2009 Prandtl-, Rayleigh-, and Rossby-number dependence of heat transport in turbulent rotating Rayleigh–Bénard convection. *Phys. Rev. Lett.* **102** (4), 044502.

ZHONG, S. 2009 Migration of Tharsis volcanism on Mars caused by differential rotation of the lithosphere. *Nat. Geosci.* **2** (1), 19–23.

ZHONG, S., ZHANG, N., LI, Z.-X. & ROBERTS, J. H. 2007 Supercontinent cycles, true polar wander, and very long-wavelength mantle convection. *Earth Planet. Sci. Lett.* **261** (3–4), 551–564.